POROUS PHOTONIC CRYSTAL EXTERNAL CAVITY LASER BIOSENSOR

BY

QINGLAN HUANG

THESIS

Submitted in partial fulfillment of the requirements
for the degree of Master of Science in Electrical and Computer Engineering
in the Graduate College of the
University of Illinois at Urbana-Champaign, 2017

Urbana, Illinois

Adviser:

Professor Brian T. Cunningham

ABSTRACT

We report the design, fabrication, and testing of a photonic crystal (PhC) biosensor structure that incorporates a porous high refractive index TiO_2 dielectric film that enables immobilization of capture proteins within an enhanced surface-area volume that spatially overlaps with the regions of resonant electromagnetic fields where biomolecular binding can produce the greatest shifts in photonic crystal resonant wavelength. Despite the nanoscale porosity of the sensor structure, the PhC slab exhibits narrowband and high efficiency resonant reflection, enabling the structure to serve as a wavelength-tunable element of an external cavity laser. In the context of sensing small molecule interactions with much larger immobilized proteins, we demonstrate that the porous structure provides 3.7× larger biosensor signals than an equivalent nonporous structure, while the external cavity laser (ECL) detection method provides capability for sensing picometer-scale shifts in the PhC resonant wavelength caused by small molecule binding. The porous ECL achieves a record high figure of merit for label-free optical biosensors.

To my family.

ACKNOWLEDGMENTS

Firstly, I would like to express my sincere gratitude to my advisor Prof. Brian T. Cunningham for the continuous support of my graduate study and research, for his immense knowledge, innovative contributions in the field of photonics and biosensing, and the wisdom in guiding graduate research. His guidance helped me throughout the research and his passion for research and life will always motivate me in my future endeavors. I could not have imagined having a better advisor for my graduate study.

Besides my advisor, I would like to thank my qualifying exam committee: Prof. Gary Eden, Prof. Stephen Boppart, and Prof. Logan Liu, for their insightful comments and encouragement, but also for the hard questions which incented me to widen my research from various perspectives.

My sincere thanks also goes to Dr. Jui-Nung Liu and Dr. Meng Zhang, who enlightened me in the first glance of research and led me into the field of nanophotonics and biosensing. Without their precious support it would not be possible to conduct this research.

I thank my fellow labmates in for the stimulating discussions, for the sleepless nights we were working together before deadlines, and for all the fun we have had in the last three years.

Last but not the least, I would like to thank my family: my parents and my sister for supporting me spiritually throughout graduate school and my life in general.

TABLE OF CONTENTS

CHAPTER 1

OPTICAL LABEL-FREE BIOSENSOR

1.1 Introduction

Measuring minute amounts of chemical and biological objects is essential for many applications ranging from medical diagnostics, drug discovery, security screening and to environmental science. In particular, screening through chemical compound libraries comprised of millions of small molecules for their potential to specifically interact with target proteins that represent key elements of disease biomolecular pathways is one of the most important methods through which new potential drugs are initially discovered [1]. Due to their low molecular weight (150-500 Da), low analyte concentration, 1:1 binding stoichiometry, and (often) low binding affinities, the ability to rapidly characterize small molecule binding with much larger proteins (20-150 kDa) remains an important technical challenge [2]. Existing methods to identify small molecule binders of nonenzymatic protein targets lack either the simplicity (e.g., require labeling one of the binding partners with a reporter) or throughput inherent in enzymatic assays widely used for high-throughput screening [3]. Thus, there is intense interest in the development of high-throughput technologies for label-free detection of protein-small molecule interactions.

Optical resonator-based biosensors have shown significant advantages for their high sensitivity and label-free operation. (Passive) optical resonators can be roughly grouped into three categories: dielectric microresonators [4], [5], plasmonic resonators [6], [7], and the emerging photonic-plasmonic hybrid resonators [8], [9], [10]. This chapter first reviews the reactive biosensing principle which underlies the majority of current optical resonator-based biosensors. Then the figure of merit (FOM) of optical resonator-based biosensors is discussed, directing to the development of active optical resonator biosensors.

Finally an overview of the most recent achievements of the field is given.

The quality factor (Q) of a resonant system quantifying the temporal confinement of the electromagnetic energy is defined as [4], [11]

$$Q = \frac{U(t)}{-\left(\frac{dU(t)}{dt}\right)/\omega_0} \tag{1.1}$$

where $U(t)$ is the total energy of the confined light field and $-(dU(t)/dt)/\omega_0$ is porportional to the energy that is lost for each electromagnetic oscillation. From this it follows that the energy of the charged cavity will decay over time with $U(t) = U_0 \exp(-\omega_0 t/Q)$ once the light source has been shut off. The ring-down time τ measured with a photodetector placed in close proximity to the resonator is $\tau = Q/\omega_0$. The exponentially decay of the energy $U(t)$ is characteristic of a resonant system. The energy $U(t)$ is proportional to the electromagnetic field strength squared $U(t) \propto E(t)^2$, and it follows that the complex field evolves in time as: $E(t) = \exp(-\omega_0 t/2Q)\exp(-i\omega|t|)$. Time and frequency domains are linked by Fourier transforms:

$$E(t) = \frac{1}{\sqrt{2\pi}} \int_{-\infty}^{\infty} E(\omega) e^{-i\omega t} d\omega \tag{1.2}$$

and we therefore expect a spectral response that exhibits a Lorentzian line:

$$|E(\omega)|^2 \propto \frac{1}{(\omega - \omega_0)^2 + (\omega_0/2Q)^2} \tag{1.3}$$

where ω_0 is the resonance wavelength and $\delta\omega = \omega_0/Q$ is the linewidth (full width at half maximum, FWHM). The wisdom behind it is that if one can figure out a means to suppress loss from either radiation or absorption (Q is enhanced), the electric field intensity can be systematically enhanced.

The optical resonator detects the presence of analyte molecules as changes in the resonance frequency. A resonator exhibits a quite large sensitivity to such perturbations if the light field is confined close to the surface where the evanescent field interacts strongly with the surrounding medium. Take the binding of a streptavidin molecule to a microsphere as an example. Note that a streptavidin molecule ($\sim$4 nm) is small with respect to the radial extension of the evanescent field associated with a whispering gallery mode (WGM) resonance. Once bound at the surface where the evanescent field strength $\mathbf{E}(\mathbf{r})$ is high, the molecule will become polarized at the optical frequency ω.

The overall induced dipole moment $\mathbf{P}$ is calculated as $\mathbf{P} = \alpha_{ex}\mathbf{E}$, where α_{ex} is the excess polarizability of streptavidin, in excess of that of the water it displaces. The energy that is needed to polarize the molecule and induce this dipole moment is $\frac{1}{2}\alpha_{ex}|\mathbf{E}(\mathbf{r_0})|^2$, where $\mathbf{E}(\mathbf{r_0})$ is the electric field strength at the streptavidin binding site $\mathbf{r_0}$, and $\alpha_{\text{ex,streptavidin}} \sim 4\pi\epsilon_0 \times 3.3 \times 10^{-21}\text{cm}^3$. By first-order perturbation theory, we can now estimate the frequency shift by comparing the energy that is needed to polarize the biomolecule to the total electromagnetic energy stored in the unperturbed resonator [12]:

$$\frac{\Delta\omega}{\omega} = -\frac{\alpha_{ex}|\mathbf{E}(\mathbf{r_0})|^2}{2\int \epsilon|\mathbf{E}(\mathbf{r})|^2 dV} \tag{1.4}$$

where ϵ is the permittivity of the medium. Equation (1.4), the reactive biosensing principle, allows one to quantify the frequency shift of any optical resonator in response to molecule or nanoparticle binding events.

A large Q factor is necessary in order to resolve the fractional frequency shift $\Delta\omega/\omega$ predicted by Eq. (1.4). In practice one monitors the resonance wavelength shift $\Delta\lambda$, which is $\Delta\lambda/\lambda = -\Delta\omega/\omega$. The limit of detection, i.e., the smallest detectable wavelength shift $\Delta\lambda_{\text{min}}$ is a fraction of $\Delta\lambda_{\text{FWHM}}$.

Importantly, the magnitude of the wavelength shift $\Delta\lambda$ itself is inversely proportional to the mode volume given by the denominator in Eq. (1.4). Reducing the modal volume of the optical resonator thus boosts sensitivity. Moreover, engineering the resonant field distribution profile to have electric field concentrated outside of the resonator itself and increase the interaction with the surrounding medium also provides an important means to enhance sensitivity.

From the above discussion, the figure of merit (FOM) of a optical resonator biosensor should capture both the Q factor and the magnitude of wavelength shift induced by biomolecule binding. The former encodes the resolution of the system and the latter reflects the refractive index sensitivity. The FOM is commonly defined as [8], [13]

$$FOM = \frac{\Delta\lambda}{\Delta n} \cdot \frac{Q}{\lambda_0} \tag{1.5}$$

Before we begin a brief survey of the most recent progresses in the field of optical label-free biosensing, it is worth pointing out that the external cavity

laser (ECL) biosensor is a fundamentally different instrumentation approach which achieves high sensitivity and high Q factor simultaneously [14]. Briefly, the stimulated emission of a semiconductor optical amplifier (SOA) generates extremely narrowband optical output ($Q = 2.8 \times 10^7$), by incorporating a PhC resonator as the wavelength tuning element of an external cavity laser. High-Q cavity is often accompanied with reduced sensitivity, as the resonant electric fields reside within solid internal regions of the biosensor structure, inaccessible to biomolecules bound to the surface of the structure. The ECL biosensor decouples the Q factor from the sensor's sensitivity by introducing external optical gain, allowing high resolution and high sensitivity simultaneously. It has been demonstrated in conjunction with photonic crystal (PhC) biosensor for pharmaceutical high-throughput screening with high specificity and sub-picometer accuracy [15], [16]. Here we report utilization of a porous PhC biosensor to even improve the sensitivity by $\sim 4\times$. The porous nanorod surface layer on the PhC provides large accessible surface area and strong interaction between the biomolecule binding volume and resonant electric field. With the lasing wavelength of 0.03 pm, this approach achieves a $FOM = 1.05 \times 10^7$, representing the record high FOM ever reported [17].

1.2 Surface Plasmon Resonance Biosensors

Surface plasmons can be excited when conduction electrons near the surface of a metallic nanostructure undergo collective oscillations coupled to an external optical field [18]. The light is slowed down and confined to the surface as a result of the coupling to the electrons. This can result in subwavelength light confinement and enhancement near the metallic surface [19], which is central to the development of new concepts in the fields of nano-optics and metamaterials. Surface plasmons are known to be extremely sensitive to the refractive index of the dielectric medium within the penetration depth of the evanescent field. This remarkable property has been used for the development of label-free plasmonic biosensors, which emerged as a leading modern technology for detection and studies of binding events between the target analyte and its corresponding receptor on a metal surface [20]. Another important consequence of the enhanced localized SPR fields is the increase in the emission, scattering, or absorption signals of molecules adsorbed on those

nanostructures. These enhancements in signal are respectively known as the surface-enhanced fluorescence effect [21], [22], surface-enhanced Raman scattering effect (SERS) [23], and surface enhanced infrared absorption effect (SEIRA) [24]. Although both effects can be used for biosensing, this thesis restricts the present discussion to plasmonics-based refractometric sensors.

SPRs can involve either "localized" electromagnetic oscillations (LSPRs) or "propagating" plasmons (PSPRs). The classical example of LSPR arises from the excitation of a single spherical gold nanoparticle by an external light field. The SPR characteristics of a spherical metallic nanoparticle, including field distribution and extinction parameters, can be obtained analytically by using the Mie scattering formalism [25]. PSPRs can be generated on a flat metallic surface. Surface plasmons are bound to the flat surface because their wavenumber is larger than that of light in the surrounding dielectric, which is similar to the situation in dielectric waveguide modes. Excitation by external light requires the momentum mismatch between light in the dielectric and light in the guided mode to be overcome, which can be achieved through prism coupling. The amplitudes of the SPR electromagnetic fields decay exponentially with distance from the surface, with a typical decay length δ_d. For PSPR on planar surfaces at visible wavelengths, δ_d is roughly of the order of half of the resonance wavelength (that is, a few hundred nanometres). For LSPR, δ_d is often significantly smaller (around 20 nm for a 30-nm-diameter spherical gold nanoparticle at the dipolar SPR resonance) [26], [27]. The resonance conditions for both LSPR and PSPR depend on the dielectric permittivity of the environment in contact to the surface of the metal. Generic SPR biosensing schemes involve the immobilization of capture molecules on the metal surface. The immobilized molecules are designed to bind preferentially to the biomolecules of interest (analytes) from the sample [28]. Therefore, although measurements of refractive index are not molecule specific, the SPR biosensor can be made highly selective to a particular biomolecule by the appropriated surface chemistry modification.

It is not our intention to make a comprehensive list of plasmonic biosensors. Rather, we would like to grasp the spirit through the discussion of two representative works on biosensing based on LSPR and PSPR, respectively.

Single-particle, single-nanohole and single-molecule sensing To achieve a sufficient sensitivity for early and robust diagnosis of health hazards such

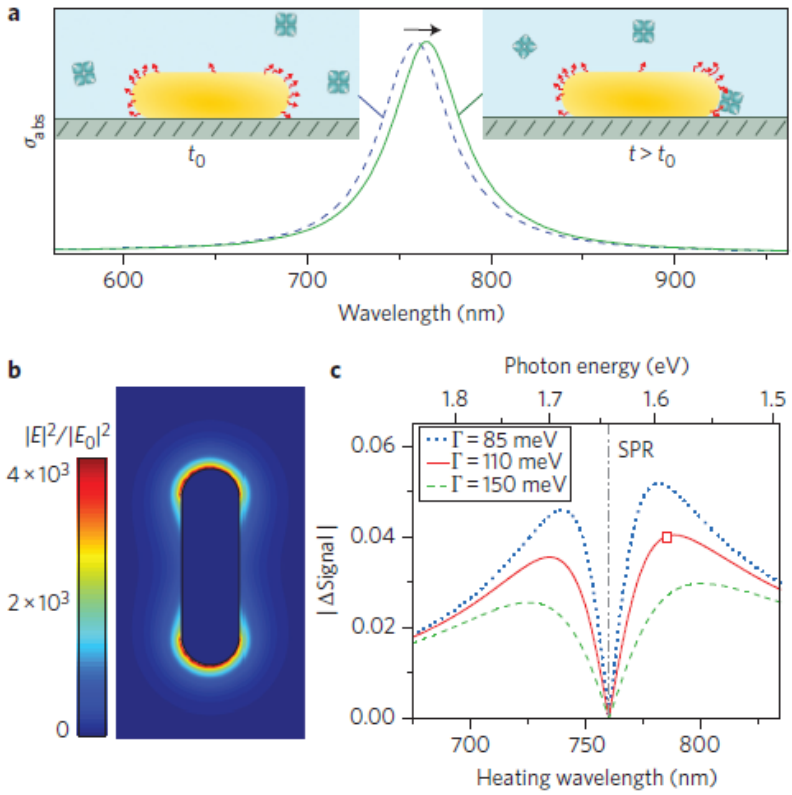

Figure 1.1: Principle of single molecule detection based on LSPR. (a) A single gold nanorod functionalized with biotin is introduced into an environment with the protein of interest. Binding of the analyte molecules to the receptors induces a redshift of the longitudinal SPR (exaggerated in the illustration). This shift is monitored at a single frequency using photothermal microscopy. (b) Calculation in the discrete dipole approximation of the electric field intensity around a gold nanorod, evaluated on resonance with its longitudinal SPR. (c) Relative change in the photothermal signal (that is, absorption cross section) as a function of the heating-laser wavelength for a redshift of 1 nm. Plotted for SPR linewidths, γ, of 85 meV (blue dotted line), 110 meV (red solid line) and 150 meV (green dashed line). The red square indicates the working point in their experiments, in which they use a heating laser with a wavelength of 785 nm. Figure adapted from [29].

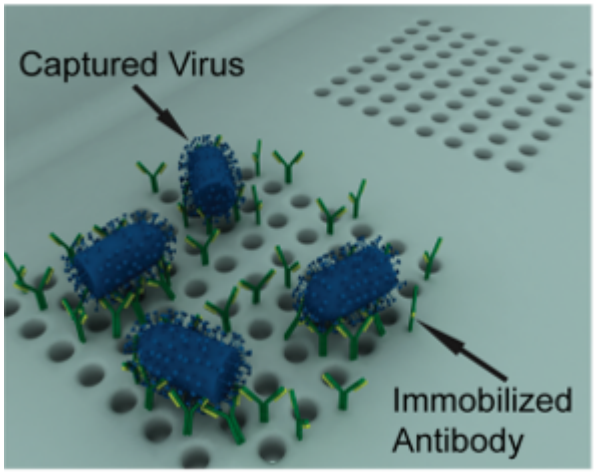

Figure 1.2: Cartoon plot of sensing platform based on an extraordinary light transmission effect in plasmonic nanoholes. Direct detection of live viruses from biological media are demonstrated via optofluidic configurations. Figure adapted from [32].

as cancer and lethal infectious disease, single molecule sensitivity is required for femtomolar range protein concentrations. Orrit et al. reported the plasmonic detection of single molecules in real time without the need for labeling or amplification [29]. Their sensor consists of a single gold nanorod coated with biotin receptor, and the binding of single proteins is detected by monitoring the plasmon resonance of the nanorod with a sensitive pothothermal assay, as shown in Figure 1.1. Photothermal microscopy relies on the change in intensity of a detection beam caused by a time-dependent thermal lens. The thermal lens is created by a modulated heating beam that is absorbed by the nanorod. When a single protein binds to the receptors on the surface of the nanorod, the longitudinal SPR shifts to the red due to the locally increased index of refraction. This shift results in a change of the absorption cross section of the nanorod at the wavelength of the heating beam. The ensuing temperature change is measured by the detection beam as a stepwise change of the photothermal signal. Figure 1.1 summarizes the principle and photothermal time trace of single-molecule binding events. Similar methods can be found in [30] and [31].

Extraordinary transmission based biosensing The observation of extraordinary transmission through a periodic array of nanoholes is a founda-

tion of a novel plasmonic detection method (Figure 1.2). External radiation is incident normally on a periodic array of nanoholes in a gold nanofilm and excites SPPs when the period is a multiple of the SPP wavelength; these SPPs carry optical energy through the holes with a high efficiency. The surface of the holey array is funcionalized by antibodies selectively binding to components (antigens) of the Ebola virus [32]. The model virus in biologically relevant concentrations is delivered by microfluidics to the surface and binds to it, decreasing the SPP velocity. The measured resonant frequency shift is very pronounced, thus demonstrating detection of this highly contagious pathogen. A similar principle is adopted in [33] for an active resonator.

1.3 Optical Microcavity Biosensors

Microcavities that support WGM resonance (microring, microsphere, microdisk, etc.), or photonic crystals (PhC), or Fabry-Perot cavities have been widely applied to biosensing. The material and geometry of a microcavity affects its Q factor as well as modal volume V and the optical field's overlap with anaylte molecules. Figures 1.3 and 1.4 give an overview for a variety of optical resonators that are currently being championed for biosensing applications.

Although most microcavity biosensors are based on reactive sensing principle, it is worth noticing that the mode-splitting effect, i.e., one resonant mode splitting into two resonances due to interaction of light with nanoscale objects, such as nanoparticles, in the mode volume, exists as an alternative principle and can be highly sensitive. WGM resonators supports degenerate counter-propagating modes: clockwise (CW) and counterclockwise (CCW). Light scattering from a scattering center introduces additional damping to the optical modes and couples the initially degenerate CW and CCW modes, lifting the mode degeneracy. A third sensing mechanism is based on loss. A WGM's linewidth is a measure of the resonator's energy loss per light wave oscillation and, as such, provides means to detect analyte species that induce addtional loss (or gain) via the associated linewidth broadening (narrowing).

A variety of photonic crystals can serve as biosensors. By introducing a point defect into a two-dimensional PhC, defect states can be pulled down from the air band or up from the substrate band. The corresponding optical

spectrum shows narrow transmission peaks inside the bandgap, whose precise position is determined by the refractive index of the pores. Unlike many sensing platforms that utilize the interaction between the small evanescent tail of the electromagnetic field and the analyte, this type of PhC localizes the electric field in the low refractive index region (e.g. air pores), which makes the sensors extremely sensitive to a small refractive index change produced by bio-molecule immobilization on the pore walls [34]. Thus, the presence of molecules inside the pores can be detected by monitoring a small spectral shift, especially if high-Q microcavities are used. Erickon et al. [35] presented a novel optofluidic biosensor platform that incorporates a unique one-dimensional photonic crystal resonator array which enables significantly stronger light-matter interaction. Coupled with the ability of planar photonic crystals to spatially localize the optical field to mode volumes on the order of a wavelength cubed, it enables a limit of detection on the order of 63 ag total bound mass. Photonic crystals based on guided mode resonance [36] utilize a grating structure to couple external light into the waveguide mode, establishing a strong electromagnetic evanescent field near the PhC surface. Refractive index change induced by biomolecule bounded on the PhC surface will result in a resonance wavelength shift.

In addition, Fabry-Perot resonators are also exploited as a biosensor [37], but with a much lower Q factor.

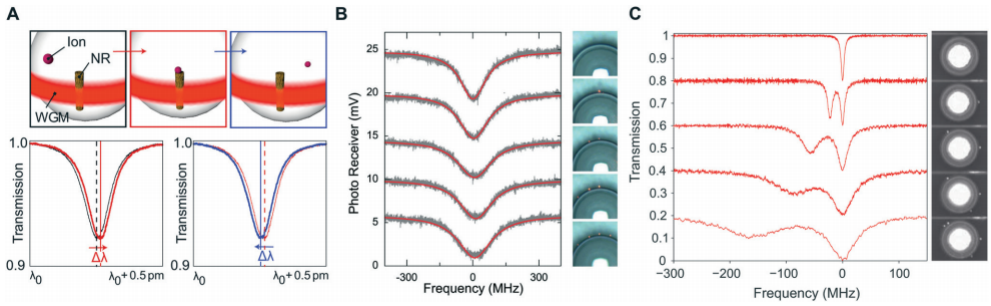

Figure 1.3: Sensing mechanisms of WGM sensors. (a) Resonance frequency shift based sensing: the spectral positions of Lorentzian WGM dips shift upon interaction of a single atomic ion with a plasmonic nanoparticle. (b) Loss based sensing: linewidth broadening of a WGM resonance dip induced by binding of polystyrene nanoparticles with 70 nm radius. (c) Mode-splitting based sensing: mode-splitting of a previously unperturbed WGM (top) as induced by successive depositions of four KCl nanoparticles with radii of 40 nm. Adapted from [38].

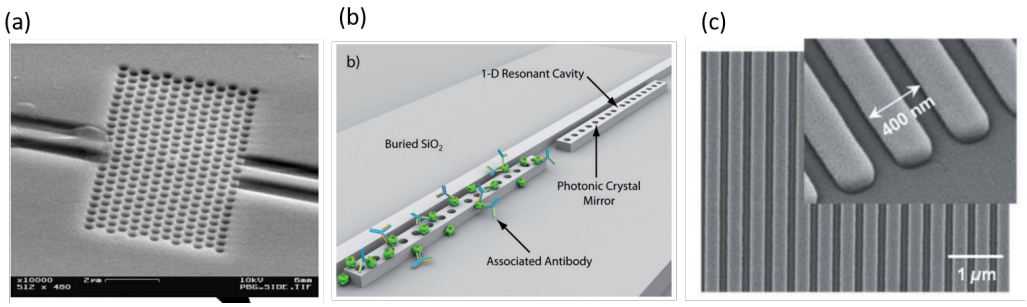

Figure 1.4: Example for photonic crystals that have been utilized or proposed for utilization in biosensing applications. (a) Two-dimensional silicon photonic crystal microcavity resonator for protein detection. Adapted from [34]. (b) Nanoscale optofluidic sensor arays, where two 1D photonic crystal resonators evanescently coupled to a silicon bus waveguide. The first resonator is immobilized with an antigen whereas the second resonator acts as a control. (c) Photonic crystal guided mode resonator featuring a one-dimensional subwavelength grating. Adapted from [36].

1.4 Photonic-Plasmonic Hybrid Resonator Biosensors

Photonic-plasmonic hybrid resonators, which incorporates the coupling between plasmonic nanoparticles and microcavity, are a new type of nanophotonic devices that attracts enormous interests. We envision hybrid structure to play an important role in surface enhanced Raman spectroscopy (SERS), fluorescence enhancement, surface enhanced infrared absorption (SEIRA), and label-free sensing. The hybrid approach to enhance the sensitivity of microcavity biosensors utilizes the fact that the frequency shift signal produced by a protein or nanoparticle binding to the microcavity is in proportion to the intensity $\mathbf{E^2}(\mathbf{r_0})$ encountered at the binding site $\mathbf{r_0}$, see Eq. (1.2). Any mechanism that can amplify the field intensity at the binding site while maintaining high Q factor will therefore produce a boost in the frequency shift signal, dramatically increasing the sensitivity in single molecule detection. Hot spots of high field intensities can be generated by evanescent coupling of the microcavity resonance to a plasmonic nanoantenna. With careful engineering of the Q factor of the microcavity, frequency overlap of the LSPR of nanoantenna and resonance of the microcavity, and the spatial location of the plasmonic nanoantenna, giant electric field enhancements can be achieved [39], [40], [41].

The first demonstration of this plasmon-enhanced microcavity detection

scheme utilized a random nanoparticle layer to generate hot spots of high field intensity after coupling to a WGM microsphere cavity [42]. High near-field enhancements were obtained by excitation of a WGM at optimal wavelength. In theory, optimized plasmon coupling can produce near-field enhancements up to three orders in magnitude, increasing the frequency shift signal for detecting a protein molecule and bringing lable-free single molecule detection within reach. For example, a nanorod immobilized on a microtoroid [43] will boost the frequency shift signal obtained for binding of a single BSA molecule into the MHz-range, which is more than an order of magnitude larger than the expected measurement noise. Recently it also has been shown that by designing the nanostructure of Au nanoshell, extra folds of wavelength shifts of WGM-nanoshell hybrid resonator [44] can be achieved, therefore bringing the protein limit of detection down to 5 kDa.

1.5 Active Resonators for Sensing Enhancement

A narrow resonance can help to resolve a small resonant shift caused by trace amount of molecules attached to the resonator, which could have been missed by a broad resonance. The resonance linewidth of a passive optical resonator, i.e., a resonator without optical gain, is limited by materials absorption loss and radiation loss of the resonator. Appropriate design of the microcavity and optimization of the fabrication process could help increase the passive Q factor, and therefore decrease the linewidth, by minimizing the radiation induced loss, but the loss from materials absorption will set the limit of the Q factor, i.e., the linewidth, for a passive resonator. However, in an active optical resonator, i.e., a resonator with optical gain, where the absorption loss can be compensated by the gain medium, the effective loss felt by the photon is decreased dramatically, which will increase the effective Q factor, subsequently decrease the linewidth, and hence improve the sensitivity and detection limit [4].

The active resonator can operate in either below-threshold and above-threshold regime; in both cases, the detection limit and resolution is significantly improved. The above-threshold regime, also termed as lasing region, in particular, is very attractive for detection purposes since the lasing line usually has a much narrower linewidth than the resonance linewidth of the cold

cavity (i.e., the gain medium is not pumped). According to the Schawlow-Townes formula, the fundamental linewidth of lasing mode in a resonator is

$$\Delta\nu_{laser} = \frac{\pi h\nu(\Delta\nu_{cold})^2}{P_{laser}} \tag{1.6}$$

where Δv_{laser} is the resonance linewidth calculated from "cold" cavity Q factor, P_{laser} is the power of the lasing mode and ν is the resonant frequency. In principle, it suggests that the microcavity laser as a sensing element could provide a much lower detection limit than its passive counterpart.

Intense interests have been developed in applying an active sensor to sensing. Figure 1.5 summarizes several examples of recent achievements in laser biosensors. Active WGM resonators have been proposed to enhance the sensitivity in the spectral shift technique. With gain medium doped polymer microspheres it is possible to detect effective refractive index change of the order of 10^{-9} RIU [45]. The active microspheres have demonstrated a minimun detection limit of 260 pg/mm^2 for a minimum detectable mass of 80 fg protein [46], or oligonucleotides [47]. Optical gain also improves the sensitivity and detection limit of mode splitting by decreasing the resonance linewidth which helps resolve the two split modes which could have otherwise appeared as one broad resonance in the spectrum [48]. Odom and colleagues reported real-time tunable lasing from plasmonic nanocavity arrays [49]. The nanolaser device is composed of optically pumped arrays of gold nanoparticles surrounded by liquid dye molecules. By integrating gold nanoparticle arrays within microfluidic channels and flowing in liquid gain materials with different refractive indices, dynamic tuning of the plasmon lasing wavelength was achieved. The scheme offers prospects to enhance and detect weak physical and chemical processes on the nanoscale in real time. Cunningham and colleagues reported a plastic distributed feedback laser biosensor using a dye-doped guided mode resonance photonic crystal slab [50], [51], [52]. A protein-protein interaction experiment demonstrated its capability to characterize antibody-antigen affinity binding constants. Simultaneous detection of refractive index and surface charges have been reported by Baba et al., using a GaInAsP photonic crystal nanolaser, based on the change in emission wavelength and intensity [53]. The pH sensing is enabled by the modification of filling of electrons at surface states of the semiconductor and hence the nonradiative surface recombination. The photonic crystal nanolaser offers

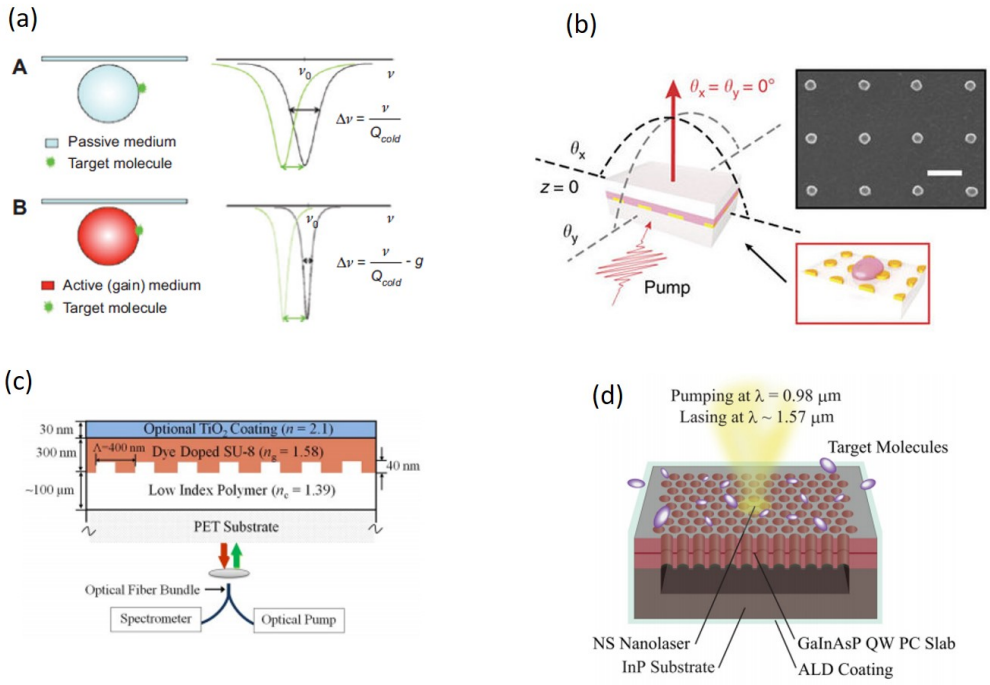

Figure 1.5: (a) The binding of molecules on the surface of a resonator shifts the resonant frequency. Compared to a passive resonator, an active resonator has narrow linewidth due to the optical gain (g), which improves the sensor resolution by reducing the smallest detectable shift in the resonance. Adapted from [4]. (b) Real-time tunable lasing from plasmonic nanocavity arrays. Adapted from [49]. (c) Plastic distributed feedback laser biosensor, adapted from [50]. (d) Simultaneous detection of refractive index and surface charges in a GaInAsP photonic crystal nanolaser, adapted from [53].

a simpler and potentially less expensive way to detect DNA hybridazation through changes in surface charge density or solution pH.

CHAPTER 2

POROUS PHOTONIC CRYSTAL EXTERNAL CAVITY LASER BIOSENSOR: PRINCIPLES

2.1 Photonic Crystal as Refractometric Sensor

Photonic crystals (PhCs) are periodic (1D, 2D, or 3D) nanostructures with extraordinary optical properties. They exhibit a complex photonic band structure of allowed (propagating) and forbidden (decaying) states in a wavelength range comparable to the length scale of their structure [54]. A schematic diagram and SEM image of our 1D PhC slab are illustrated in Figure 2.1 and Figure 2.2. It is comprised of a single layer of TiO_2 thin film on top of a one-dimensional subwavelength grating structured ultraviolet curable polymer (UVCP). The period $\Lambda = 550$ nm, grating depth $t_{\text{grating}} = 170$ nm, $n_{\text{TiO2}} = 2.4$ and $n_{\text{UVCP}} = 1.5$. The device is fabricated on a flexible, transparent plastic substrate, so that the incident light could illuminate the PhC from the substrate side, providing freedom for solution operation. We choose the PhC to operate in solution and has resonance in the NIR range (850 nm) since the water has low absorbance in the NIR window. The layer thickness d and period Λ control the peak-background ratio, linewidth, and spectral location of the resonance, thereby enabling facile design and fabrication of different PhCs.

Here we adopt the analytical model developed by Liu [55] and Ganesh [56] to grasp the physical insight of its behavior. When illuminated by a broadband source, the coupling between the incident light and the periodic subwavelength structure occurs via a phase-matching condition. The light couples into and out of the in-plane guided mode resonance supported by the structure via first-order Bragg scattering:

$$\mathbf{k}_{\text{mode}} = \hat{x}|\mathbf{k}_0|\sin\theta_i \pm \mathbf{G}_x \tag{2.1}$$

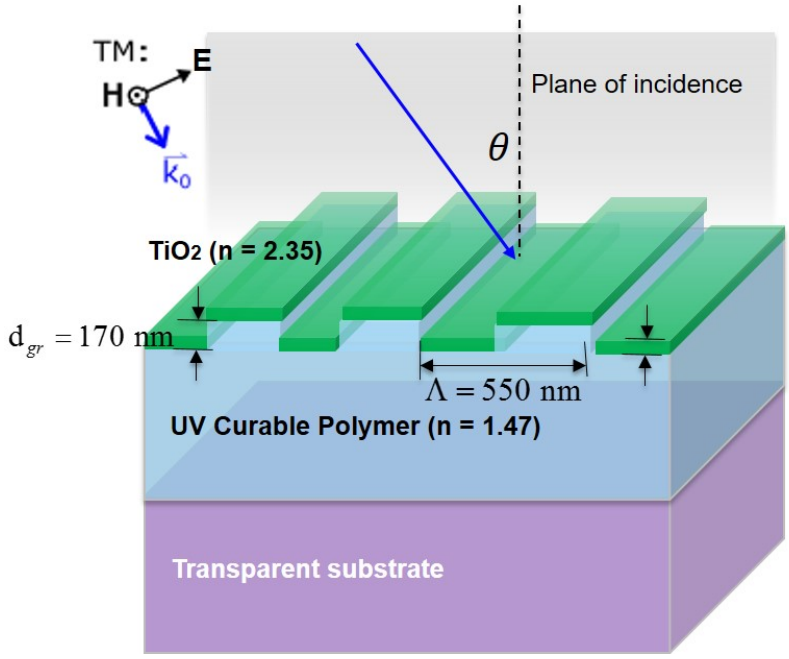

Figure 2.1: Schematic diagram of guided mode resonance photonic crystal. The incident field is transverse magnetic (TM) polarized.

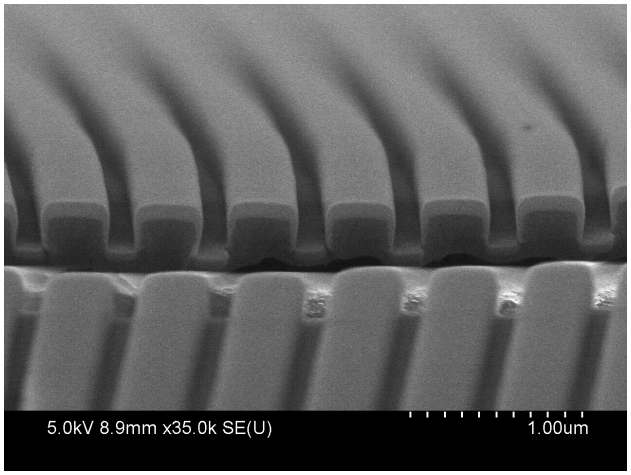

Figure 2.2: Scanning electron microscopy image of the NIR PhC.

where $\mathbf{k}_{\text{mode}}$ is the wavevector of a specific guided mode, $\hat{x}$ is the unit vector in the x direction, $\mathbf{k}_0 = \frac{2\pi}{\lambda}$ is the wavevector of the incident light, and $\mathbf{G}_x = \frac{2\pi}{\Lambda}$ is the reciprocal lattice vector. This mechanism creates a sharp resonance peak in the spectra (resonant Wood's anomalies).

The TiO_2 thickness determines the guided mode dispersion $\mathbf{k}_{\text{mode}}$. By ignoring the grating ripples, the TiO_2 thin layer can be approximated as a flat slab waveguide with thickness d. The guided modes can be computed using the dielectric waveguide theory [57]. The eigenequations for the guidance condition for a guided mode with a wavenumber m in a dielectric slab with a thickness d are:

$$\begin{aligned}\sqrt{(n_{\text{TiO2}}k_0)^2 - k_{\text{mode}}^2}d = &tan^{-1}\left(\frac{\alpha_{\text{water}}}{\sqrt{(n_{\text{TiO2}}k_0)^2 - k_{\text{mode}}^2}}\right) + \\ &tan^{-1}\left(\frac{\alpha_{\text{sub}}}{\sqrt{(n_{\text{sub}}k_0)^2 - k_{\text{mode}}^2}}\right) + m\pi\end{aligned} \tag{2.2}$$

for TE_m mode, and

$$\begin{aligned}\sqrt{(n_{\text{TiO2}}k_0)^2 - k_{\text{mode}}^2}d = &tan^{-1}\left(\frac{n_{\text{TiO2}}^2}{n_{\text{water}}^2}\frac{\alpha_{\text{water}}}{\sqrt{(n_{\text{TiO2}}k_0)^2 - k_{\text{mode}}^2}}\right) + \\ &tan^{-1}\left(\frac{n_{\text{TiO2}}^2}{n_{\text{sub}}^2}\frac{\alpha_{\text{sub}}}{\sqrt{(n_{\text{sub}}k_0)^2 - k_{\text{mode}}^2}}\right) + m\pi\end{aligned} \tag{2.3}$$

for TM_m mode. The α_{water} and α_{sub} are the decay constants in the transverse direction in water and substrate, respectively, and are defined as

$$\alpha_{\text{water}} = \sqrt{k_{\text{mode}}^2 - (n_{\text{water}}k_0)^2} \tag{2.4}$$

$$\alpha_{\text{sub}} = \sqrt{k_{\text{mode}}^2 - (n_{\text{sub}}k_0)^2} \tag{2.5}$$

Figure 2.3 shows the analytical computed dispersion curve and cutoff for the TiO_2 slab waveguide. Here we choose $d = 110$ nm to match the SEM image of the cross section of the device, and fundamental-mode (TE_0 and

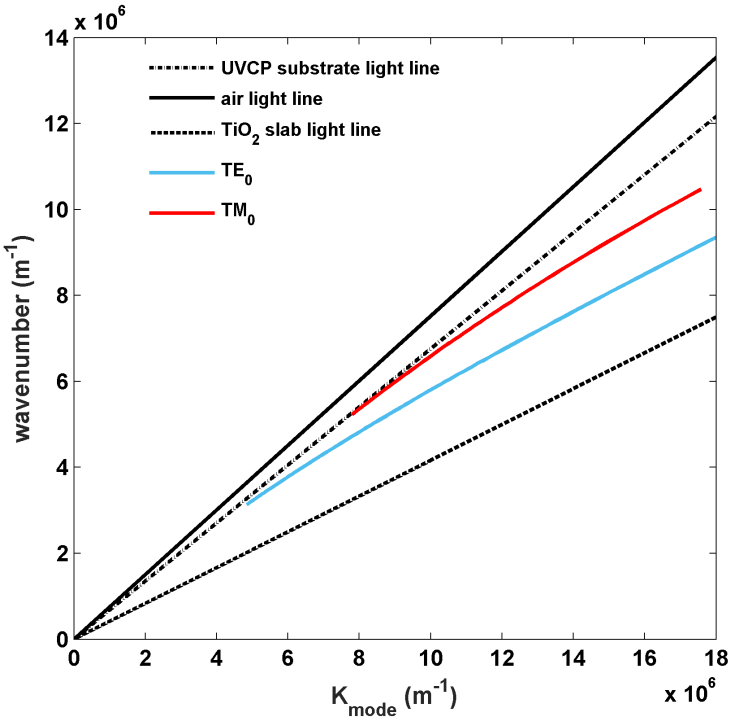

Figure 2.3: Calculated dispersion curves of two fundamental waveguide modes, TE_0 and TM_0 with $d = 110$ nm.

TM_0) operation. The resonance wavelength can be predicted analytically based on the momentum-matching condition Eq. (2.1) or the given period. The dispersion curves starts at the cutoff on the substrate light line ($k_{\text{mode}} = k_0 n_{\text{UVCP}}$) and approaches the slab light line ($k_{\text{mode}} = k_0 n_{\text{TiO2}}$) for higher wavenumber limit. The normally incident light aquires a momentum of $2\pi/\Lambda$ in the x direction and couples to the guided mode dispersion based on the phase-matching condition $\mathbf{k}_{\text{mode}} = \pm\mathbf{G}_x$. The analytical value matches the experimentally measured value very well. For $\Lambda = 550$ nm, $\lambda_{\text{res}} = 852$ nm, whereas the measured value is 852 nm.

The guided mode resonance, defined by a complex propagation constant, possesses a finite lifetime and is re-radiated into free space to form a narrow band reflection. Therefore, the near-field electromagnetic (EM) field enhancement is associated with a farfield resonant reflection peak. We utilize the TM_0 mode as it has a narrower resonance peak as compared to TE_0. The measured transmission spectrum of the PhC at normal incidence is shown in Figure 2.4. The PhC shows a narrow (FWHM = 5 nm) and high contrast reflection peak (transmission dip). As the refractive index (RI) of the super-

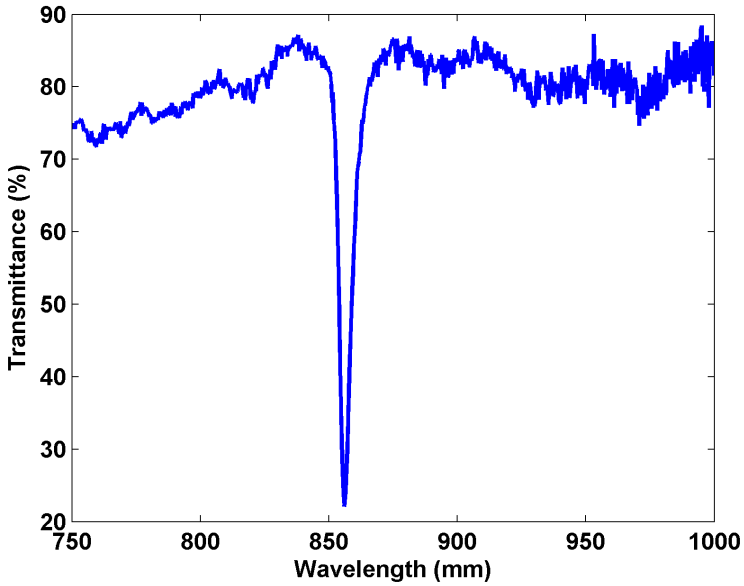

Figure 2.4: Measured transmission spectrum of PhC. The incident white light is TM polarized and illuminates the PhC at normal incidence.

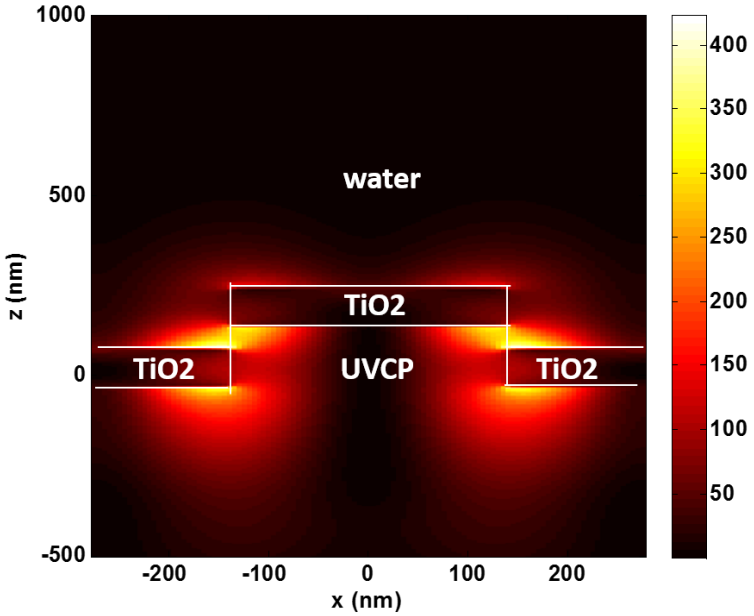

Figure 2.5: Electric field intensity $|\mathbf{E}|^2$ profile of PhC immersed in water, at $\lambda = 851$ nm. The incident light is TM polarized and illuminates the PhC at normal incidence.

strate changes, the PhC experiences a resonance red shift, as higher RI light line pushes the dispersion curve toward the TiO_2 light line. By changing the liquid covering the PhC with DMSO solution of different concentrations, the resonance wavelength can be tuned continuously in a wide dynamic range, in a linear fashion. The bulk sensitivity is characterized to be 212 nm/RIU.

At resonance, energy associated with the light is temporarily stored in the resonator and the surrounding medium in the form of an electromagnetic standing wave with an evanescent reduction in intensity as one moves in the z-direction into the media (Figure 2.5). The resonant fields induce dipole moments in biomolecules within the evanescent field volume. As bound proteins and small molecules displace water, we observe a shift in the photon energy of the resonant state. As discussed in Chapter 1, a biosensor would be in favor of having a highly intense evanescent field to overlap with the analyte bound to the PhC surface. Here, we introduce the porous PhC to boost sensitivity.

2.2 Porous Photonic Crystal Enhances Sensitivity

Here we report utilization of a porous PhC biosensor in which a nanorod TiO_2 layer is used to improve sensitivity by 3.7 times. Different from the slab, solid PhC described previously, the porous PhC has a TiO_2 nanorod layer on the surface, forming a porous film that enhances the interaction between biomolecules and the PhC resonator [58], [59], [60].

The porous PhC is a one-dimensional grating structure fabricated on a low refractive index, ultra-violet curable polymer (UVCP) (Λ = 550 nm; t_{grating} = 170 nm; n_{UVCP} = 1.5), which is coated with two layers of TiO_2 thin films (Figure 2.6). Following the sputtering of the first solid TiO_2 layer (n_{TiO_2} = 2.4; d_{TiO_2} = 75 nm), a layer of porous TiO_2 nanorod film is formed by glancing angle deposition (GLAD). GLAD is a physical vapor deposition technique that employs glancing-angle incidence to achieve porous thin films with very high surface area [61]. It was performed in an e-beam deposition system (Denton Vacuum) with a base pressure of 2.0×10^{-6} Torr and a deposition rate of 8 Å/s. The sensor was tilted so that the incoming flux of evaporated material is at a glancing angle of $\theta = 3.0°$ from the sensor surface, as shown in Figure 2.7(c). A random growth fluctuation in the

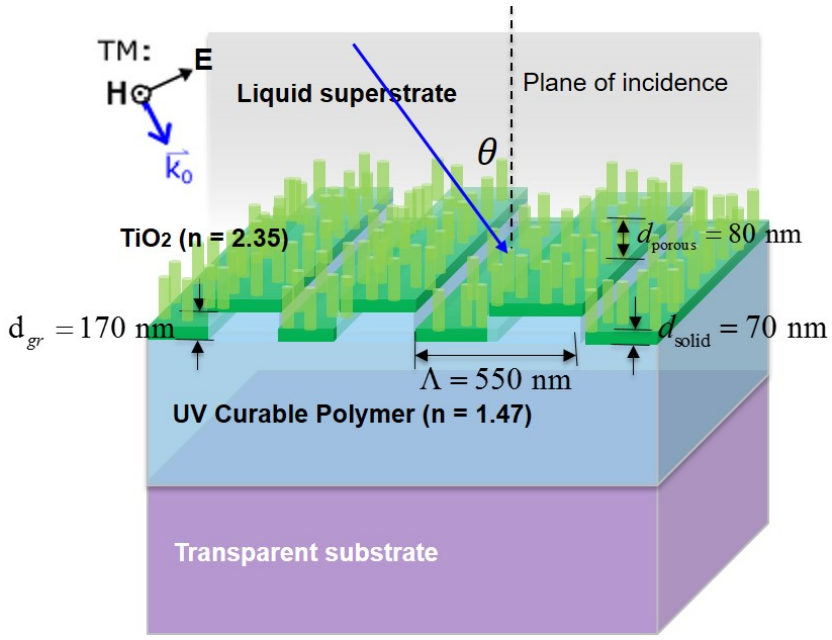

Figure 2.6: Schematic diagram of guided mode resonance photonic crystal. The incident field is transverse magnetic (TM) polarized.

substrate produces shadowed regions that the subsequent incident vapor flux cannot reach. When the mobility of adaatoms is limited, this self-shadowing effect during deposition results in a film with a structure composed of isolated vertical nanorods tilted toward the incoming flux. This technique has been used in various applications in optical and semiconductor devices. In order to minimize the shadowing effect between grating lines, the incoming flux must be parallel to the grating sidewalls so no substarte rotation is used during deposition. As shown in the scanning electron microscopic images of the top (Figure 2.7(a)) and cross-sectional (Figure 2.7(b)) views of the device, the porous layer is a uniform sheet of tilted TiO_2 nanorods with a height of ~ 80 nm and a lean angle of $\sim 35°$. Next, dry etch using CF4 (PlasmaLab Freon RIE) is performed to slightly expand the gaps between TiO_2 nanorods. The etch step is important, as gaps between nanorods of greater than 20 nm are required to enable protein molecules to diffuse into the pores and to bind within the structure, rather than simply attaching to the upper surface of the porous layer. Figure 2.8 shows how the porosity is controlled during device fabrication and effects of porosity on experimental sensitivity. The porous PhC is designed to function in aqueous media, with water perfused between nanorods.

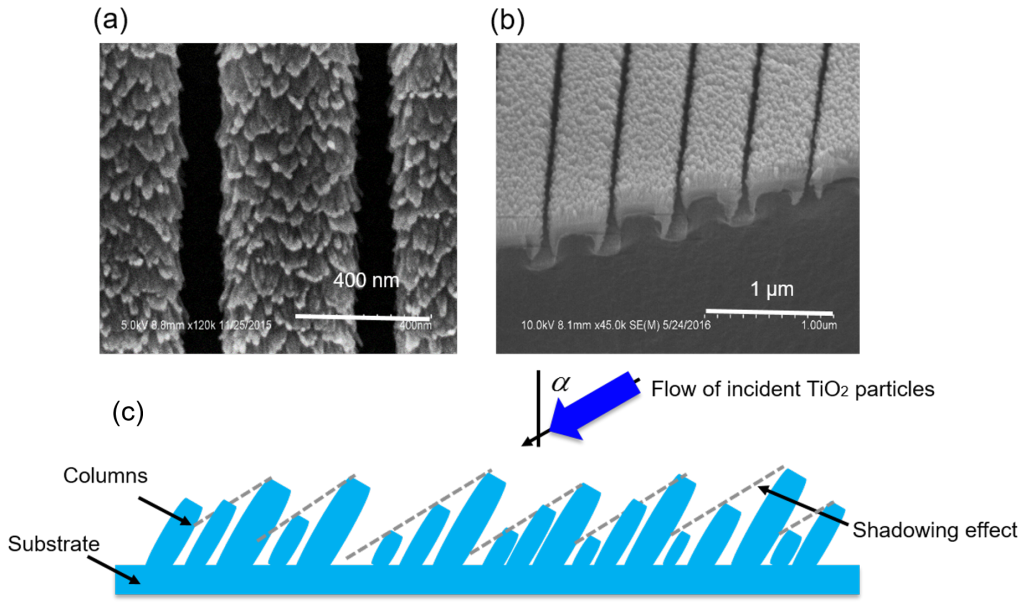

Figure 2.7: Scanning electron microscopy images of the PhC with a porous TiO_2 nanorod layer surface (a), and tilted view (b). (c) Cartoon depicting the principle of glancing angle deposition. The incoming flux incident the substrate at a tilted angle. A random growth fluctuation in the substrate produces a self-shadowing effect, resulting in discrete, oblique nano pillars to form.

At resonance, the subwavelength grating couples the external incident light to excite a guided mode resonance (GMR) as described in Section 2.1. The GMR, defined by a complex propagation constant, possesses a finite lifetime and is re-radiated into free space to form a narrow band reflection. Therefore, the near-field electromagnetic (EM) field enhancement is associated with a farfield resonant reflection peak. As shown in the reflection spectrum in Figure 2.9, the porous PhC reflects a narrow range of wavelengths centered at $\lambda_{\text{res}} = 851$ nm, with FWHM = 5 nm. Because the features of the nanorods are far smaller than the resonant wavelength, the nanorod layer does not cause scattering or absorption that results in extinguishing the resonance. Compared with non-porous PhCs, the porous PhCs do not result in significant broadening or shortening of the resonant peak, which is vital to establishing lasing action in the ECL system.

Now we analyze the sensitivity enhancement mechanism of the porous PhC and estimate the enhancement factor as compared to nonporous PhC described in Section 2.1. By first-order perturbation theory, the fractional

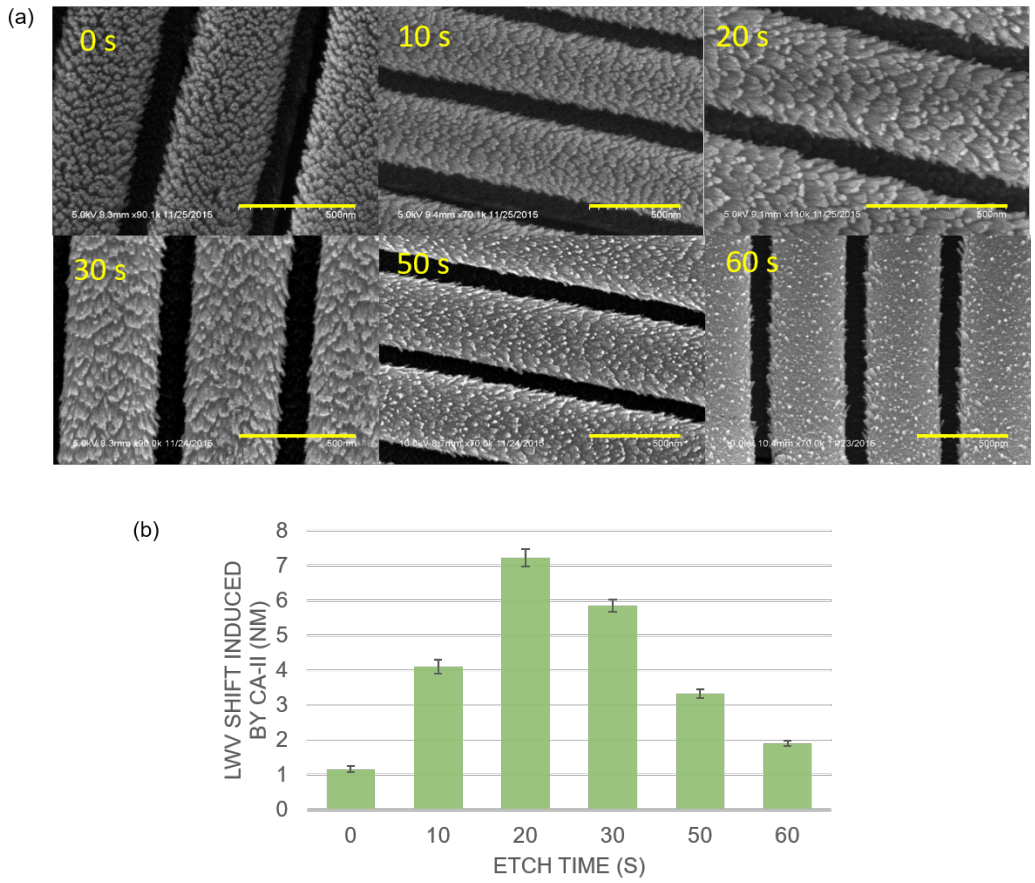

Figure 2.8: Tuning of porosity and effects on sensitivity (a) SEM images of porous PhCs with RIE treatment for times ranging from 0-60 sec. Scale bar: 500 nm. (b) LWV shifts induced by protein CA-II during the surface chemistry step for a series of porous PhCs with different etch times (different porosity). Error bars represent for the standard deviation from four independent sensors.

resonant wavelength shift from a large number of molecules bound on optical resonators can be estimated as the ratio of the energy needed to polarize and induce dipole moments in the molecules and the total energy of the mode

$$\frac{\Delta\lambda}{\lambda} = \frac{\alpha_{\mathrm{ex}}\sigma_{\mathrm{p}} \int |\mathbf{E}(\mathbf{r})|^2 dA}{2 \int \epsilon |\mathbf{E}(\mathbf{r})|^2 dV} \tag{2.6}$$

where α_{ex} is the molecules' excess polarizability to water, σ_{p} is the protein surface density, A is the surface area where binding events occur, and V is the mode volume. Equation 2.6 provides physical insight on how can one increase the refractive index sensitivity. It reveals that one can increase the

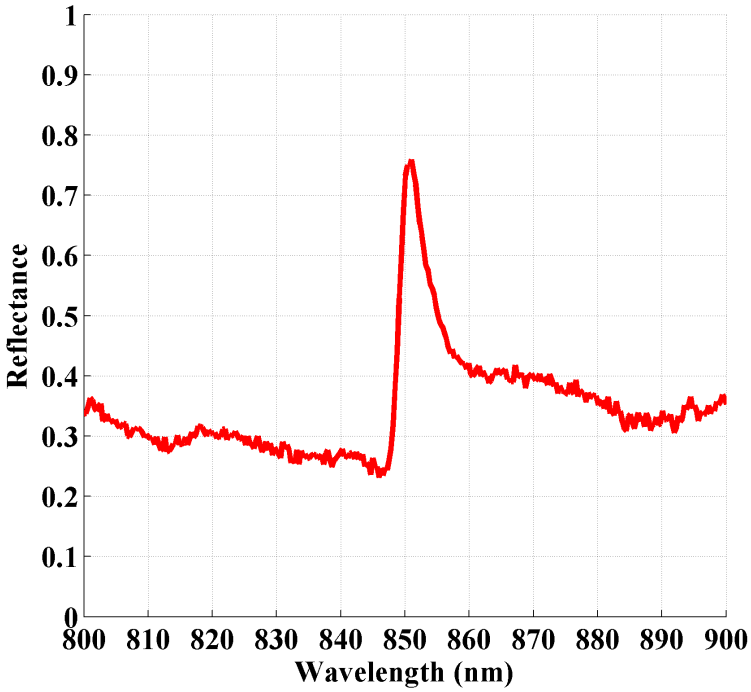

Figure 2.9: Measured reflection spectrum when the porous PhC is covered with water, with TM polarized normal incident light.

interaction of biomolecules and the PhC biosensor by (1) providing large surface area to accommodate the surface bounding events, allowing efficient mode overlap with the biomolecular binding volume; (2) creating electric field "hot spot" on the surface of the resonator, or making the resonant field concentrates outside of the solid resonator itself to interact with the target analytes.

The porous PhC boosts sensitivity by both mechanisms. First, the nanorods extrude the originally flat surface into a three-dimensional (3D) volume within the evanescent field region and increase the surface area, in a manner similar to porous silicon biosensors [62]. We estimate a surface enhancement factor as follows. With the measured refractive index (RI) of the porous layer 1.40, which is the weighted average RI of TiO_2 and air in space, the volume ratio of the two materials can be approximated as 0.3:0.7. Then, nanorods can be approximated as an array of 40 nm diameter cylinders with 25 nm wide gaps and 80 nm height. Compared to a flat surface, the extra surface area provided by cylinder sidewalls can be calculated. Thus, a maximum 3.4× enhancement in the surface area is expected. However, because protein

molecules occupy 3D volumes that will prevent close-packed occupation of all the available surface area (for example, two proteins may not fit in one gap between neighboring rods), we cannot expect the surface area enhancement to correlate precisely with the density of immobilized capture proteins in the structure. The extended surface area is accompanied by efficient projection of the evanescent field onto the biomolecule binding volume. The resonant electric field intensity profile calculated by the finite difference time domain (FDTD) method (Lumerical) is shown in Figure 2.10, where the porous layer is modeled as a uniform dielectric layer with measured RI of the layer. The evanescent field tail extends to around 200 nm above the sensor surface and overlaps with the porous layer. Each location in the porous 3D biomolecule binding volume contributes totuning the resonance wavelength, whereas in the nonporous PhCs, only the electric field within a 30 nm-thin conformal sheet covering the PhC surface interacts with the biomolecules, and a large portion of the evanescent field above the 30 nm threshold is not exploited to participate in biosensing.

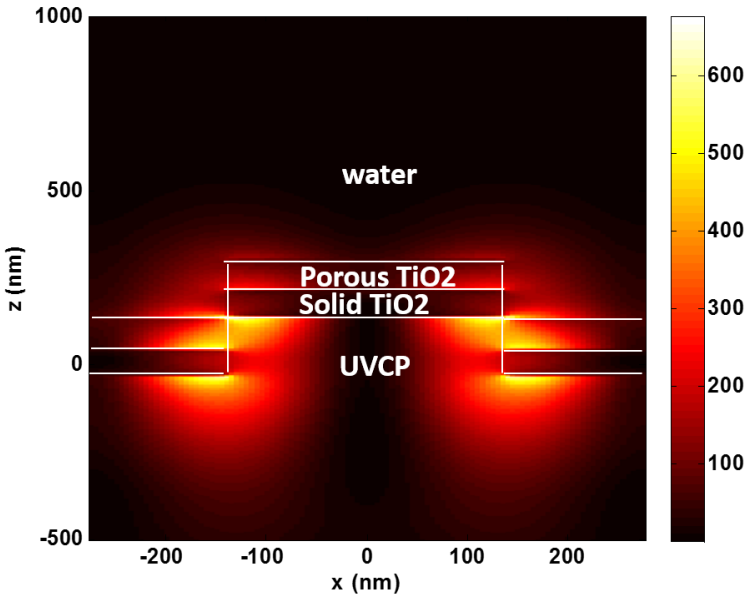

Figure 2.10: FDTD computed near electric field intensity profile $|\mathbf{E}|^2$ for normally unit incident plain wave for the TM resonant mode at $\lambda = 851$ nm.

Second, the porous layer modifies the resonant mode profile and increases the electric field intensity especially in the porous layer, enlarging the nu-

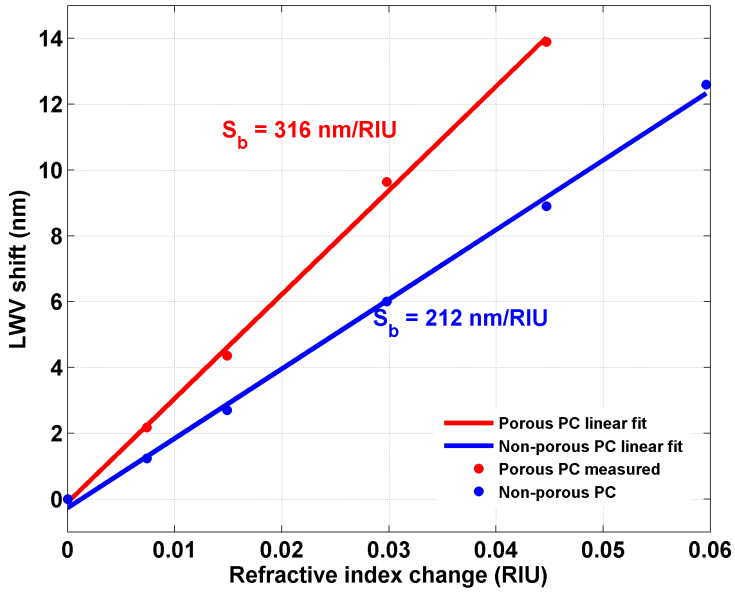

Figure 2.11: Bulk sensitivity comparison between porous and non-porous PhCs. Laser emission wavelength shifts of both sensors exposed to water: DMSO solution with different refractive index. A linear fit to the experimentally obtained data reveals a bulk sensitivity of 212 nm/RIU for non-porous PhCs and 316 nm/RIU for porous PhCs.

merator in Eq. (2.6). This can be shown by comparing the near field of the porous PhC (Figure 2.10) and nonporous PhC (Figure 2.5). The porous PhC provides higher electric field intensity than nonporous PhC. Meanwhile, with a porous layer, the evanescent field extends to a considerably larger volume above the solid dielectric. The absolute shift value can be estimated from Eq. (2.6) if the E field magnitude is known everywhere in the porous layer. In our FDTD model, to save computation resources, the discrete TiO_2 nanorods and water pores in between are not taken into account, instead a uniform RI layer is used to represent the weighted average of TiO_2 and water. This configuration reflects the resonant spectrum and coarse mode distribution but does not provide nanometer-scale spatial resolution of the E field magnitude in the TiO_2 nanorods and in the water pores in between. To demonstrate this phenomenon experimentally, we compare the bulk refractive sensitivity of the porous and nonporous PhCs. By exposing each PhC surface to a series of water: DMSO (Dimethyl sulfoxide) mixtures over a range of DMSO concentrations, we determine the bulk sensitivity of the porous PhC to be

316 nm/RIU, while the bulk sensitivity of a nonporous PhC is 212 nm/RIU. The bulk sensitivity comparison is shown in Figure 2.11. Therefore, the field profile mechanism contributes to approximately 1.5× the wavelength shift induced for a fixed change in dielectric permittivity for the material added to the sensor surface or porous volume.

2.3 External Cavity Laser for High Q Factor

External cavity laser (ECL) is featured for its tunable wavelength and narrow emission linewidth. It is composed of a laser diode chip that typically has one facet anti-reflection coated, and a wavelength-selective optical element, to provide narrowband optical feedback. Three elements are required for a laser to operate: (1) an active gain medium that amplifies the optical signal, (2) a feedback mechanism to provide sustained laser oscillation, and (3) a pump to provide population inversion.

In a Fabry-Perot laser, two mirros having a reflection coefficient r_1 and r_2 (power reflectance $R_1 = r_1^2$ and $R_2 = r_2^2$) provide feedback for the optical field. The round-trip gain for the optical field within a cavity of length L can be expressed as [57]

$$\sqrt{G_{rt}} = (r_1 r_2) e^{(g-\alpha_i)L} e^{-j\frac{2\pi}{\lambda} n_{eff} 2L} \tag{2.7}$$

where g and α_i are the gain and internal loss coefficients, respectively, λ is the vacuum wavelength, n_{eff} is the effective refractive index, and L is the cavity length. Solving for unity results in the threshold amplitude and phase conditions:

$$g_{th} = \alpha_i + \frac{1}{2L} ln \frac{1}{R_1 R_2} = \alpha_i + \alpha_m \tag{2.8}$$

$$\lambda_N = \frac{2 n_{eff} L}{N} \tag{2.9}$$

where α_m is defined as the mirror loss and N is a running integer index representing the mode number.

In a semiconductor laser, the gain medium is excited by injecting a current into the junction region of a forward biased diode. The high concentration of electrons and holes in the engineered quantum-well junction of a semiconductor laser makes it possible to create the population inversion required

for optical gain. A Fabry-Perot cavity can be created by the Fresnel optical reflections at the cleaved facets of the chip. The junction is effectively a waveguide that extends from one facet to the other. An uncoated "as-cleaved" facet perpendicular to the waveguide has a reflectivity of $R \sim 30\%$. To accomplish this, a wavelength-selective feedback element external to the semiconductor laser chip can be used to select the lasing wavelength. Proper operation of this external cavity laser (ECL) requires suppression of the intrinsic optical feedback from the semiconductor chip Fabry-Perot cavity so that it does not interfere with the external feedback. The gain chip's Fabry-Perot cavity effect can be reduced by applying an antireflection (AR) optical coating to the chip facets.

The emission spectrum of the Fabry-Perot laser diode device will be dependent on the injection current. When biased below threshold with $g > \alpha_i$ the emission spectrum consists of a broad series of peaks corresponding to the longitudinal modes of the Fabry-Perot cavity defined by the phase equation. Lasing does not occur until the injection current is increased to the point where $g = \alpha_i + \alpha_m$. The evolution of laser oscillation is shown in Figure 2.12. The lasing wavelength is determined by the longitudinal mode that first achieves the threshold condition [63]. The output spectrum does not always collapse into a single lasing wavelength but can consist of a narrow spectrum of longitudinal modes.

The linewidth of a semiconductor laser single longitudinal lasing mode (FWHM) is given by the modified Schawlow and Townes formula:

$$\Delta\nu_{laser} = \frac{\pi h\nu(\Delta\nu_{cold})^2}{P_{laser}} \tag{2.10}$$

where Δv_{laser} is the resonance linewidth calculated from "cold" cavity Q factor, P_{laser} is the power of the lasing mode and ν is the resonant frequency.

There are numerous approaches for implementing an external cavity semiconductor laser. One of the most common feedback elements is a diffraction grating, which can be used as the feedback element in both single-wavelength and broadly tunable external cavity lasers. Littrow configuration and Littman-Metcalf configuration are the two most popular ECL implementations.

Here in our external laser cavity biosensor, the PhC resonant reflector acts as the transducer upon which biological material is adsorbed, which also

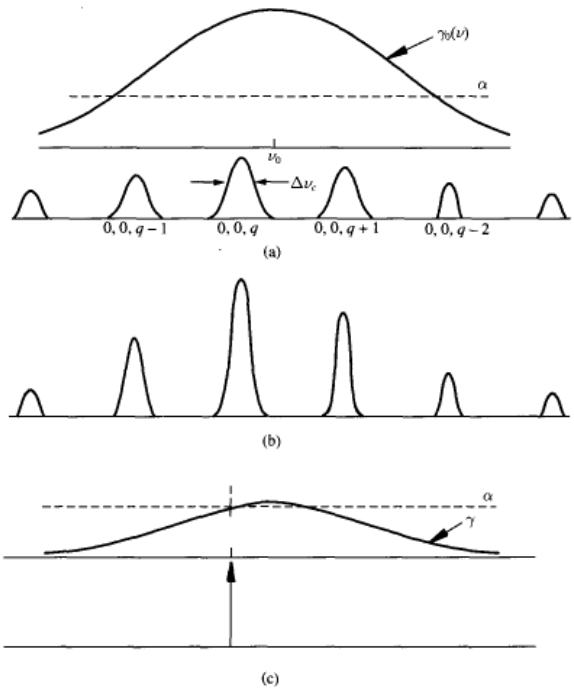

Figure 2.12: Evolution of laser oscillation from spontaneous emission: (a) initial; (b) intermediate; and (c) final. Figure adapted from [63].

serves as the wavelength selective element of the external cavity laser (ECL). The process of stimulated emission of an external optical gain realizes an active optical cavity that achieves narrow bandwidth continuous wave light output. An optical fiber-coupled traveling-wave semiconductor optical amplifier (SOA) is used as the gain media, which illuminates the PhC at normal incidence. The PhC reflects a narrow band of wavelengths through the optical fiber and provides feedback to the SOA, establishing a laser cavity whose emission wavelength is tuned by the adsorption of biomaterial on the PhC surface. Importantly, the smooth gain spectrum of the SOA and the length of the external cavity (determined by the length of the optical fiber) result in apparently continuous tuning of the lasing wavelength without abrupt hops between modes. The FOM of this approach, as shown in Table 2.1, is greater than previously published passive resonator biosensors due to the high Q factor of the ECL emission (2.8×10^7) [14] and the high refractive index sensitivity of the (porous) PhC resonator.

As shown in Figure 2.13, the ECL biosensor comprises an SOA, two polarization maintaining single-mode optical fibers, a near-infrared (NIR) mirror, a porous PhC resonator, and an instrument for measuring laser wavelength.

Table 2.1: Figure of merit comparison with other optical label-free sensors

Methods	Linewidth (nm)	S_b (nm/RIU)	FOM
Porous ECL (this work)	3×10^{-5}	316	1.05×10^7
ECL [14]	3×10^{-5}	212	7.06×10^6
Plasmonic ECL [33]	2.1×10^{-2}	547	2.60×10^4
Plamonic nanocavity lasers [49]	1.5	2150	1.43×10^3
Single nanobeam [13]	15	631	9.50×10^3
PhC nanolaser[64]	2.60×10^{-5}	350	1.34×10^4
PhC biosensor [36]	3	2112	71
Microsphere [4]	5×10^{-4}	26	5.2×10^4
Microring [4]	5×10^{-2}	140	2800
SPR [65]	80	970	12

The SOA (SAL-372, Superlum Inc., $\lambda_0 = 850$ nm and a 3-dB bandwidth of $\Delta\lambda = 40$ nm) has both edge facets coated with anti-reflection layers ($R < 10^{-3}$) with a tilted waveguide design to obtain a gain ripple as low as 0.2 dB. Each end facet of the SOA is coupled to a single-mode polarization maintaining fiber with a length of 1m.

The light coming from one end of the fiber is reflected against the mirror, while light from the other output of the SOA is directed by a collimator to illuminate two adjacent sensors at normal incidence from below. The polarization of the incident light from the polarizing maintaining (PM) fiber is adjusted so that the s and p polarized light from the polarizing beam splitter (PBS) have equal intensity. The halfwave plate ensures that both beams are polarized perpendicular to the PhC gratings. The reflection of the porous PhC is coupled back into the laser cavity, where it is amplified by the SOA. An active optical resonator with two resonant modes is established through the stimulated emission process, and a shutter alternates between excitation of the "active" and "reference" sensor. The two optical paths are set for difference measurements in order to suppress common mode noise including thermal drift and nonspecific binding. The details of the self-referening noise reduction will be discussed soon in Section 2.4.

The mode spacing is given by $\Delta\lambda_m \approx \frac{\lambda^2}{2(n_0 l_0 + n_g l_g + n_{SOA} l_{SOA})}$ [14], where m is the mode number, λ_m is the m^{th} longitudinal mode wavelength, λ is the center wavelength, and $n_0, n_g, n_{SOA}, l_0, l_g, l_{SOA}$ are the effective refractive

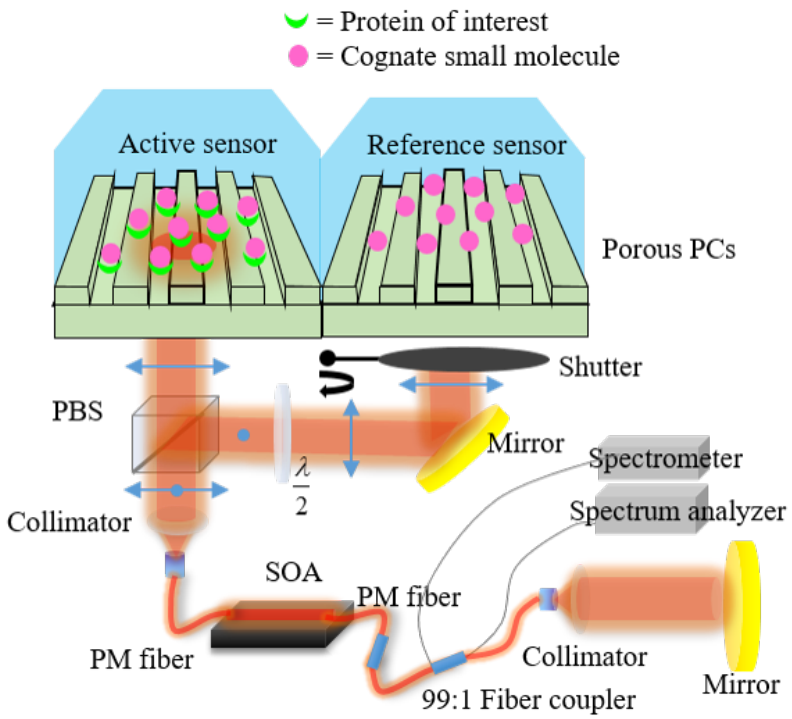

Figure 2.13: Schematic diagram of the external cavity laser biosensor system. An optical fiber-coupled traveling-wave semiconductor optical amplifier (SOA) is used as the gain media, which illuminates the PhC at normal incidence. The PhC resonant reflector acts as the transducer upon which biological material is adsorbed, which also serves as the wavelength selective element of the external cavity laser (ECL). A pulse driven bistable shutter enables alternate operation of the active and reference lasing mode with 0.5 Hz frequency.

index and length of the air, single-mode fiber, and the SOA cavity, resulting in a cavity length that is dominated by the length of the optical fiber. By using two 1 m single-mode fibers, a longitudinal mode spacing of 0.08 pm is estimated, representing the smallest increment in wavelength shift that can be obtained. This ensures continuous tuning of lasing wavelength without abrupt hops between modes. To enable single-mode operation, we set the injuction current at 70 mA, a value just above the lasing threshold (62 mA). Under this condition, only the PhC reflection peak and a narrow range of wavelength around the peak will be efficiently coupled into the single-mode fiber and the gain chip within the acceptance angle of the waveguide. The coupled light gets amplified inside the gain chip multiple times, depending on the Q factor of the cold cavity. This amplification process transfers the

initially relatively wide reflection peak into a much narrower peak. The lasing wavelength depends on the first longitudinal mode that achieves the threshold condition and is tuned by the absorption of biomolecules on the PhC surface.

The output spectra of the ECL system collected from the above sensors, shown in Figure 2.14, clearly demonstrate the porous PhCs' wavelength selection function. The raised background represents the broadband SOA spontaneous emission, where the porous PhC resonance registers a transmission dip at the center of the SOA gain spectrum near $\lambda = 855$ nm. The dynamics of establishing lasing behavior is illustrated by three curves, representing the output below (red), just above (blue), and well above (green) the lasing threshold, respectively. Above the threshold, a laser emission occurs at the transmission dip, overlapping with the porous PhC resonance. The relative broad PhC resonant reflection peak translates into a narrow laser emission spike via the process of stimulated emission. The laser output surpasses the spontaneous emission and gradually increases intensity with increasing injection current. The laser output power is approximately 1 mW, which is considerably lower than passive WGM biosensors or other active pulse pumped optical sensors [52]. A precise calibration of the ECL laser emission using a scanning Fabry-Perot interferometer demonstrated single-mode lasing with a FWHM of 0.03 pm [14]. The narrow linewidth enables resonant wavelength shifts to be resolved with sub-picometer accuracy. Therefore, the porous ECL establishes a record high FOM of 1.05×10^7.

The fiber coupler couples 1% of the light from the cavity to LabVIEW controlled dual-measurement instruments to monitor binding events in real time. A spectrum analyzer (Model 721, Bristol Instruments, Inc., 0.2 pm resolution) tracks the peak lasing wavelength. We implement repeated testing of the laser wavelength value (LWV), in which serial N (=10 in this work) independent LWV measurements taken at 50 ms intervals are averaged to generate a "final" LWV with a resolution of $0.2/N^{1/2}$ pm (0.06 pm). A spectrometer (HR 4000, Ocean optics, 20 pm resolution) enables observation of the spectrum to verify single mode operation.

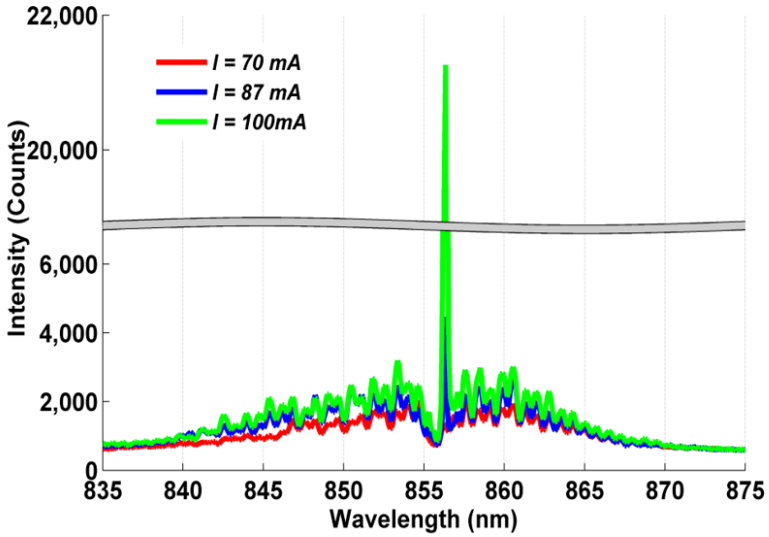

Figure 2.14: Spectra of the ECL system output light (collected from above a porous PhC sensor) with injection current under (red), just above (blue), and well above (green) the threshold. Here, the porous PhC is immersed in water: DMSO solution.

2.4 Self-Referencing for Noise Suppressing

Challenges confronting the detection of ECL biosensor resonance wavelength, as well as many other label-free biosensors, are the detection of noise signal which is indistinguishable from the actual binding event. For example, thermal fluctuations in the test sample, thermal-induced refractive index changes in the PhC resonator or the SOA material, thermal expansion/contraction of the sensor material, as well as nonspecific binding of biomaterials to the sensor surface, can cause wavelength drift on a similar magnitude to the wavelength shift that is induced by actual protein-small molecule interactions [16], [15]. Incorporation of self-referencing is key to enable direct detection of small molecule binding to immobilized protein targets.

In analogy to differential amplifiers in analog circuits, two PhC sensors in adjacent wells of a 96-well plate were utilized as the sensing elements in the ECL cavity at the same time. Each sensor selects its own resonant wavelength, so the ECL system can lase at two independent wavelengths simultaneously. Self-referencing was accomplished by designating one well as the "reference" well and the other as the "active" well, where both sensors were fabricated identically on the same substrate and were prepared iden-

tically with exception of the immobilized protein in the active well. Due to the close physical proximity of the active and reference sensors, accurate referencing is achieved to compensate for common mode noise. Importantly, the active and reference laser cavities share the entire optical system, including the gain medium, optical fibers, and mechanical holding stages, thus any common-mode error that may cause the lasing wavelength to drift will occur to both devices in an identical fashion. Moreover, the side-by-side configuration of the active and reference sensors enables the use of a pulse-driven bistable shutter for alternate operation of the two lasing modes with a frequency of 0.5 Hz. This avoids competition between two simultaneously oscillating modes and enables stable operation of the ECL system. By kinetically monitoring the laser wavelength values (LWVs) of the alternating lasing modes, a self-referenced LWV shift was obtained by subtracting the LWV of the reference sensor from the active sensor, resulting in an effectively reduced noise level with a short-term standard deviation of $\sigma = 0.8$ pm over a 20 min time period [16], [15]. Moreover, the LWV variations of the active sensor have a fluctuation range of 15 pm (Figure 2.15), demonstrating the importance of the reference sensor.

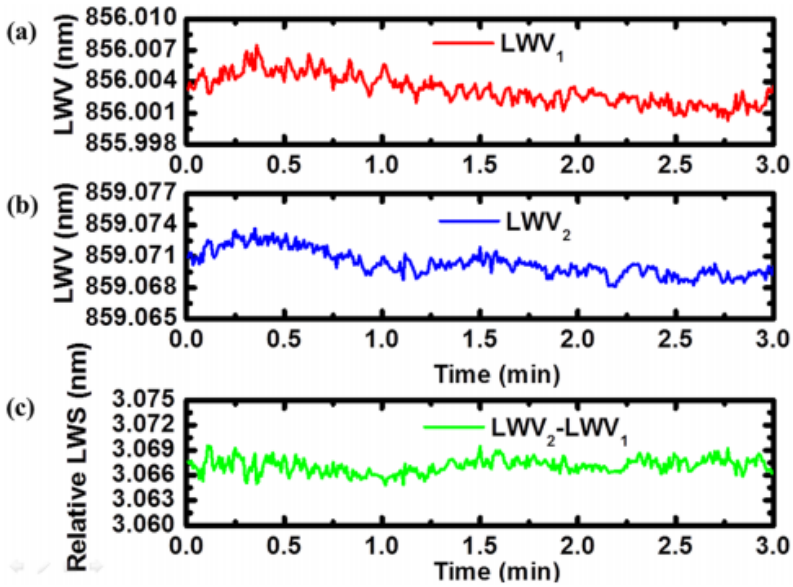

Figure 2.15: Dual-mode emission wavelengths as a function of time demonstrating the stability of the dual-mode ECL system and the ability to correct for the effects of small environmental fluctuations. Temporal variation of lasing wavelength values from (a) top PhC and (b) bottom PhC mode with DI water. (c) Relative laser wavelength shift shows a short-term standard deviation of 0.8 pm for this 3-min measurement. Figure adapted from [15].

CHAPTER 3

DETECTION OF PROTEIN-SMALL MOLECULE INTERACTION

3.1 Materials and Methods

To compare sensitivity between sensors with and without the nanorod coating, a three-step assay protocal was performed, as shown in Figure 3.1, intended to demonstrate how the available sensor surface area interacts with different types of molecules. PhC biosensor surface was functionalized first with a polyvinylamine layer (PVA; provided by SRU Biosystems Inc.) that can conform to the available exposed surface area in a single monolayer. The polymer consists of a long, narrow molecular chain with a high density of amine (NH_2) functional groups available along its backbone. The polymer adheres to the TiO_2 sensor surface by noncovalent interaction, and is considered to be small enough to fit between adjacent rods in the nanorods film. Therefore, the LWV shift measured during attachment of the PVA layer should reflect the enhancement of surface area due to the nanorod film. The sensor was immersed in a 0.625% PVA solution in 1× PBS and incubated at 37 °C for 28 h. The wells were then washed thrice with 1× PBS, followed by a measurement of LWV shift.

The second step of the protocol involves functionalizing the amine groups within the deposited polymer films with glutaraldehyde (GA). Due to the small molecular weight of GA, it is also expected to penetrate the nanorod surface structure. The GA will form a stable covalent attachment to the polymer amine groups. The chemical structure of GA allows the molecule to perform as a bifunctional linker, allowing for subsequent protein molecules bound with exposed amine moieties. The wells were incubated with a 25% GA solution in 1× PBS for 4 h, followed by a was step and a measurement of PWV shift.

To immobilize the protein of interest onto the biosensor surface, 40 μL

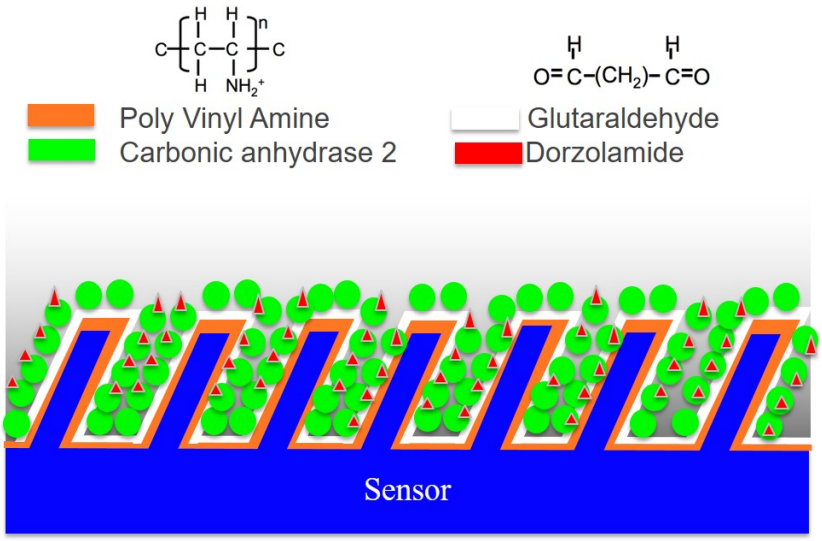

Figure 3.1: Protein CA II and its cognate small molecule dorzolamide binding assays. The porous PhCs and nonporous PhCs are treated sequentially with polyvinylamine (PVA), which provides amine functional group, Glutaraldehyde (GA), which is a bi-functional linker, and CA II, which bound covalently to GA. Dorzolamide solution is added in the final step.

of 0.5 mg/mL of protein solution was added to each of the active well and incubated overnight at 4 °C. Bovine carbonic anhydrase isozyme II (CA II, 29 kDa) were diluted in 1× PBS pH 7.4. After an overnight incubation, the wells were washed once to remove excess unbound protein and kept in PBS at 4 °C until they were used. LWV shift of the protein incubation step was performed before applying small molecules.

Figure 3.1 compares the LWV shifts of porous and nonporous PhC sensors in each of the surface chemistry step. The error bars represent the standard deviation of three identical sensors measured independently for each condition. In each step, $\sim 4\times$ larger LWV shifts were obtained with porous PhCs. This result indicates higher sensitivity for the porous PhCs, and higher density of capture proteins immobilized on the porous PhCs.

3.2 Small Molecule and Protein Interaction Results

The cognate small molecule of CA II is dorzolamide (324 Da), and they have a dissociation constant of $K_D = 1.1$ nM. Dorzolamide was dissolved in

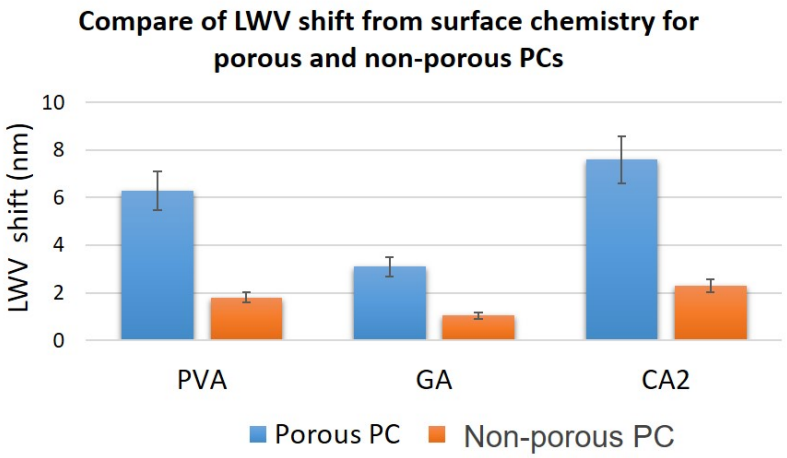

Figure 3.2: Improved sensitivity of the porous PhCs as compared to non-porous PhCs. Laser wavelength value (LWV) shifts for porous and non-porous PhCs after each step of the surface chemistry process. The error bars represent the standard deviation of three independent sensors.

DMSO. The small molecules were added at a final concentration of 50 μM in 5% DMSO into both the active and reference wells. The concentration is well above the K_D value, so as to saturate the available binding sites on immobilized CA II. Because our system does not utilize microfluidic flow (the liquid in contact with the sensor is static), the kinetic binding characteristic measurement is limited by diffusion of molecules to the biosensor surface, rather than by the chemical binding interaction that is typically used to measure K_D. The sensor plate was read for 20 min at RT.

The kinetic LWV shift as a function of time for both sensors is shown in Figure 3.3. A LWV shift of 52 pm is observed in the porous PhCs, while a shift of only 14 pm occurs in the non-porous PhCs. The 3.7× enhancement in the wavelength shift corresponds well with the wavelength shift enhancement in the first three surface chemistry steps and is expected due to the 1:1 binding stoichiometry of dorzolamide to its attachment site on the CA II protein. Both curves are the difference between the LWV shifts in the active and reference wells and represent the "net" signals associated with actual biomolecule binding. Both resonant shifts induced by dorzolamide are greater than three standard deviations (3σ) of the noise. This result shows the considerably higher signal-to-noise ratio and sensitivity offered by the porous PhCs. The 3.7× enhanced wavelength shift magnitude difference between the two types of PhCs occurs by a combination of enhanced surface

area (which results in more CA II capture protein immobilized within the porous TiO_2 than the density of capture protein that can bind upon a "flat" nonporous layer) and greater interaction between the PhC resonant mode and the volume in which biomolecules attach, which we characterized as a 1.5 sensitivity enhancement via the bulk refractive index sensitivity.

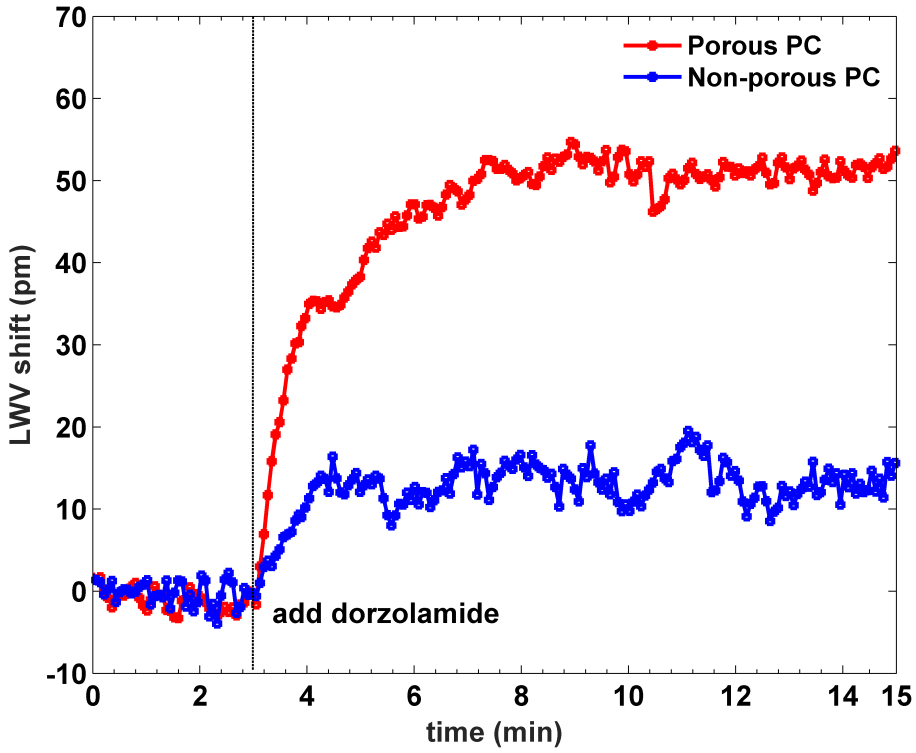

Figure 3.3: Observed kinetic LWV shift for the CA II - dorzolamide interaction, for the porous PhC (red) and non-porous PhC (blue) sensors. The vertical dotted line indicates the addition of dorzolamide to both the active and reference wells.

CHAPTER 4

CONCLUSIONS AND OUTLOOK

4.1 Conclusions

Detection of small molecule modulators of various macromolecular targets is a critical early component of pharmaceutical screening and the new drug discovery process. The well-established approaches including colorimetric or fluorimetric activity assays are more amenable to enzymatic inhibitors. However existing methods to identify small molecule binders of nonenzymatic protein targets lack either simplicity or throughput. Here a label-free technology for detection of protein-small molecule interactions is demonstrated. Due to the size of small molecules, the detection of wavelength shift of optical resonators generated by protein-small molecule interaction requires a sensor with high sensitivity and high resolution. Figure of merit (FOM) is a measure of sensitivity and resolution.

This thesis described an external cavity laser biosensor in conjunction with a porous photonic crystal. A nanorod-coated porous PhC based on guided mode resonance was designed and fabricated for kinetically detect protein-small molecule-binding interactions. The porous PhCs deliver 3.7× higher sensitivity than non-porous sensors through a combination of their enhanced surface area and effective utilization of the resonant electric field. The porous PhC functions as a wavelength selective mirror of an external cavity laser. Detection of protein-small molecule events tunes the ECL emission wavelength. The semiconductor optical amplifier provides optical gain for the laser and transfers a relatively broad PhC resonant reflection peak into a narrow lasing mode via the process of stimulated emission. This optical label-free biosensor achieves a record high FOM of 1.05 $\times 10^7$.

Proof of concept experiment was carried out for kinetic monitoring of dorzolamide interacting with protein CA II. Self-referencing difference measure-

ment suppresses common mode noise including thermal drift and nonspecific binding. A dynamic binding graph shows that the porous PhC resonator delivers almost 4× higher laser wavelength shift and thus higher signal-to-noise ratio as compared to their nonporous counterparts.

4.2 Future Work

The future work will focus on improving the sensitivity by combining plasmonic nanoparticles (NPs) with a PhC resonator to achieve hybrid photonic-plasmonic resonators. Synergistic operation between the plasmonic NPs and the PhC microresonator can be achieved by judiciously choosing the NP surface density and Q-factor of the PhC, as governed by the Q-matching mechanism in antenna theory. Upon resonance, the plasmonic and photonic modes couple together in synergy. The PhC provides optical feedback to the NPs, suppressing its dissipation rate and hence increasing its Q_{abs}. As a result, giant enhancement of near-field intensity appears at the surroundings of NPs. This modification of near-field spatial distribution, i.e., significant increase in the field in the area accessible by the protein molecules in the PhC-NP structure is expected to translate into the larger sensitivity of the hybrid PhC-NP sensor. In the frame of the first-order perturbation approximation, fractional wavelength shift of the mode caused by a small protein molecule with a real excess polarizability a at position $\mathbf{r}_\mu$ is directly proportional to the field intensity value at the molecule position $|\mathbf{E}(\mathbf{r}_\mu)|$ and inversely proportional to the energy density integrated over the whole mode volume.

Figure 4.1 summarizes several recent demonstration of hybrid resonators in sensing application. Maier et al. [8] demonstrated a hybrid nanoparticle-microcavity-based plasmonic nanosensors with improved detection resolution and extended remote-sensing ability. Coupling of a strong dipolar plasmonic resonance of a single gold nanoparticle to the narrow bandwidth resonances of a Fabry-Perot optical microcavity creates a hybrid mode and discretizes the broad localized resonance, boosting the sensing figure of merit (FOM) by up to 36 times. Chanda et al. [9] revealed the coupling of a quasi-three-dimensional plasmonic crystals with an underlying Fabry-Perot type cavities. This arrangement could lead to strongly enhanced or diminished

reflections (∼23 dB change), due to significant modifications in the nature of the plasmonic modes, in a way that could be tuned reversibly using the techniques of opto-fluidics. Associated amplification in the surface plasmon field lead to modulation of signal levels in surface-enhanced Raman scattering (SERS) experiments up to 4×. Arnold and colleagues [44] reported the label-free detection of single proteins using a nanoplasmonic-photonic hybrid microcavity. The single molecule sensitivity is achieved through the strong reactive field intensity near the surface of the Au nanoshell receptor, due to its intrinsic random bumps of protein size. Odom and colleagues [66] reported a Rayleigh anomoly based subradiant plasmon with a narrow (∼ 5 nm) resonant linewidth formed by a two-dimensional gold naoparticle array. At resonance, strong coupling between out-of-plane nanoparticle dipolar moments supresses radiative decay, trapping light in the plane of the array and strongly localizing optical fields on each nanoparticle. This can be seem as another type of optical cavity in the sense that it provide optical feedback to the plasmonic resonator. Goldsmith et al. [39] presented a new single-particle double-modulation photothermal absorption spectroscopy method that employs on-chip optical WGM microresonators as ultrasensitive thermometers. Their single gold nanorods detection revieals a dense array of sharp Fano resonances arising from the coupling between the localized surface plasmon of the gold nanorod and the WGMs of the resonator. Fabrizio et al. [67] hybridized a nobel metal nanowaveguide to a photonic crystal cavity. Raman scattering of single inorganic nanopariticles or monolayers of organic compunds can be detected.

In the PhC-NP scheme, critical questions need to be answered by numerical simulation first: (1) to demonstrate sensitivity enhancement by using hybrid resonator as compared to PhC resonator; (2) to determine the appropriate LSPR resonance spectral location with respect to PhC resonance, i.e., whether the two resonance should overlap or offset by certain amount; (3) to determine NP surface density with which the hybrid resonator can operate in synergy. The reflection intensity, that is, the lasing capability of the hybrid cavity also needs to be taken into consideration.

After we design the hybrid system for label-free sensing, experimental demonstration on refractive index sensing will be carried out. Devices will be fabricated using quartz substrate, and NP with appropriate LSPR will be chemically grown and applied to the PhC surface, with the collaboration of

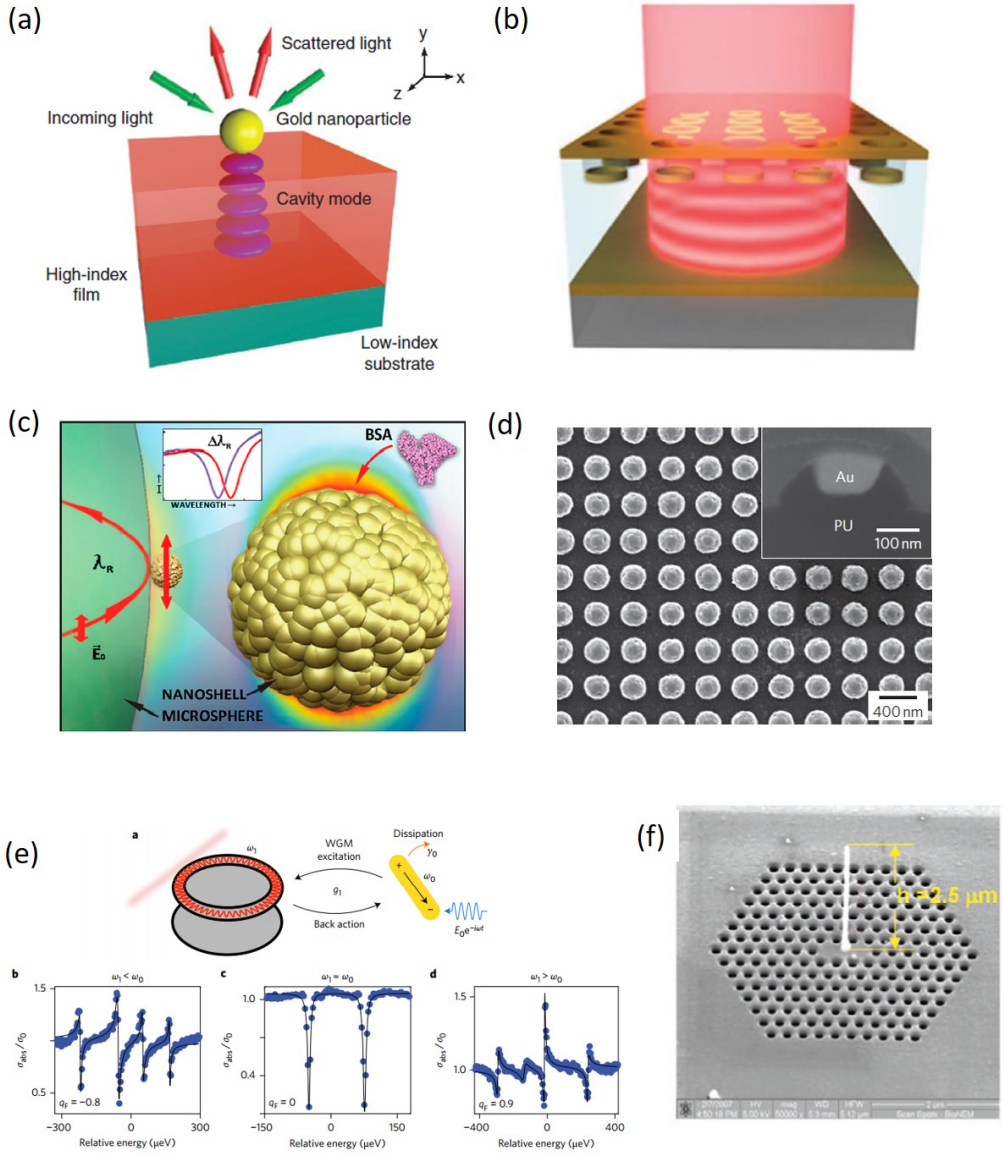

Figure 4.1: Representative examples in plasmonic-photonic hybrid resonator sensors, adapted from [8]. (a) Gold nanoparticle coupled to a Fabry-Perot cavity. (b) Plasmonic crystals coupled to a Fabry-Perot cavity, adapted from [9]. (c) Nanoshell coupled to a WGM microcavity, adapted from [44]. (d) Subradiant lattice plasmons formed by gold nanoparticle arrays, adapted from [66]. (e) Gold nanorod coupled to WGM mode, establishing Fano interference, adapted from [39]. (f) Plasmonic nanowaveguides coupled to a photonic crystal cavity, adapted from [67].

University of Washington. Bulk refractive index sensitivity will be characterized, and lasing of ECL needs to be demonstrated. Finally, protein-small molecule detection assay will be carried out.

REFERENCES

[1] J. Bajorath, "Integration of virtual and high-throughput screening," *Nature Reviews Drug Discovery*, vol. 1, no. 11, pp. 882–894, 2002.

[2] J. W.-H. Li and J. C. Vederas, "Drug discovery and natural products: End of an era or an endless frontier?" *Science*, vol. 325, no. 5937, pp. 161–165, Sep 2009.

[3] L. N. Makley and J. E. Gestwicki, "Expanding the number of druggable targets: Non-enzymes and protein-protein interactions," *Chemical Biology and Drug Design*, vol. 81, no. 1, pp. 22–32, 2012.

[4] F. Vollmer and L. Yang, "Review label-free detection with high-q microcavities: A review of biosensing mechanisms for integrated devices," *Nanophotonics*, vol. 1, no. 3-4, Jan 2012.

[5] D. Threm, Y. Nazirizadeh, and M. Gerken, "Photonic crystal biosensors towards on-chip integration," *Journal of Biophotonics*, vol. 5, no. 8-9, p. 601616, Aug 2012.

[6] A. G. Brolo, "Plasmonics for future biosensors," *Nature Photonics*, vol. 6, no. 11, p. 709713, May 2012.

[7] T. W. Odom and G. C. Schatz, "Introduction to plasmonics," *Chemical Reviews*, vol. 111, no. 6, pp. 3667–3668, Aug 2011.

[8] M. A. Schmidt, D. Y. Lei, L. Wondraczek, V. Nazabal, and S. A. Maier, "Hybrid nanoparticle microcavity based plasmonic nanosensors with improved detection resolution and extended remote-sensing ability," *Nature Communications*, vol. 3, p. 1108, Sep 2012.

[9] D. Chanda, K. Shigeta, T. Truong, E. Lui, A. Mihi, M. Schulmerich, P. V. Braun, R. Bhargava, and J. A. Rogers, "Coupling of plasmonic and optical cavity modes in quasi-three-dimensional plasmonic crystals," *Nature Communications*, vol. 2, p. 479, 2011.

[10] F. Vollmer, D. Braun, A. Libchaber, M. Khoshsima, I. Teraoka, and S. Arnold, "Protein detection by optical shift of a resonant microcavity," *Applied Physics Letters*, vol. 80, no. 21, pp. 4057–4059, 2002.

[11] H. A. Haus, *Waves and Fields in Optoelectronics*. Prentince-Hall, Inc., 1984.

[12] S. Arnold, M. Khoshsima, I. Teraoka, S. Holler, and F. Vollmer, "Shift of whispering-gallery modes in microspheres by protein adsorption," *Optics Letters*, vol. 28, no. 4, p. 272, 2003.

[13] S. Kim, H.-M. Kim, and Y.-H. Lee, "Single nanobeam optical sensor with a high Q-factor and high sensitivity," *Optics Letters*, vol. 40, no. 22, p. 5351, Oct 2015.

[14] C. Ge, M. Lu, S. George, T. A. Flood, C. Wagner, J. Zheng, A. Pokhriyal, J. G. Eden, P. J. Hergenrother, B. T. Cunningham, and et al., "External cavity laser biosensor," *Lab on a Chip*, vol. 13, no. 7, p. 1247, 2013.

[15] M. Zhang, C. Ge, M. Lu, Z. Zhang, and B. T. Cunningham, "A self-referencing biosensor based upon a dual-mode external cavity laser," *Applied Physics Letters*, vol. 102, no. 21, p. 213701, 2013.

[16] M. Zhang, J. Peh, P. J. Hergenrother, and B. T. Cunningham, "Detection of protein small molecule binding using a self-referencing external cavity laser biosensor," *Journal of the American Chemical Society*, vol. 136, no. 16, pp. 5840–5843, 2014.

[17] Q. Huang, J. Peh, P. J. Hergenrother, and B. T. Cunningham, "Porous photonic crystal external cavity laser biosensor," *Applied Physics Letters*, vol. 109, no. 7, p. 071103, 2016.

[18] E. Ozbay, "Plasmonics: Merging photonics and electronics at nanoscale dimensions," *Science*, vol. 311, no. 5758, pp. 189–193, 2006.

[19] D. K. Gramotnev and S. I. Bozhevolnyi, "Plasmonics beyond the diffraction limit," *Nature Photonics*, vol. 4, no. 2, pp. 83–91, 2010.

[20] A. V. Kabashin, P. Evans, S. Pastkovsky, W. Hendren, G. A. Wurtz, R. Atkinson, R. Pollard, V. A. Podolskiy, and A. V. Zayats, "Plasmonic nanorod metamaterials for biosensing," *Nature Materials*, vol. 8, no. 11, pp. 867–871, Nov 2009.

[21] A. Kinkhabwala, Z. Yu, S. Fan, Y. Avlasevich, K. Mllen, and W. E. Moerner, "Large single-molecule fluorescence enhancements produced by a bowtie nanoantenna," *Nature Photonics*, vol. 3, no. 11, pp. 654–657, 2009.

[22] K. J. Russell, T.-L. Liu, S. Cui, and E. L. Hu, "Large spontaneous emission enhancement in plasmonic nanocavities," *Nature Photonics*, vol. 6, no. 7, pp. 459–462, 2012.

[23] P. L. Stiles, J. A. Dieringer, N. C. Shah, and R. P. V. Duyne, "Surface-enhanced Raman spectroscopy," *Annual Review of Analytical Chemistry*, vol. 1, no. 1, pp. 601–626, 2008.

[24] L. V. Brown, X. Yang, K. Zhao, B. Y. Zheng, P. Nordlander, and N. J. Halas, "Fan-shaped gold nanoantennas above reflective substrates for surface-enhanced infrared absorption (SEIRA)," *Nano Letters*, vol. 15, no. 2, pp. 1272–1280, Nov 2015.

[25] K. L. Kelly, E. Coronado, L. L. Zhao, and G. C. Schatz, "The optical properties of metal nanoparticles: The influence of size, shape, and dielectric environment," *The Journal of Physical Chemistry B*, vol. 107, no. 3, pp. 668–677, 2003.

[26] E. Ringe, B. Sharma, A.-I. Henry, L. D. Marks, and R. P. V. Duyne, "Single nanoparticle plasmonics," *Physical Chemistry Chemical Physics*, vol. 15, no. 12, p. 4110, 2013.

[27] K. M. Mayer and J. H. Hafner, "Localized surface plasmon resonance sensors," *Chemical Reviews*, vol. 111, no. 6, pp. 3828–3857, Aug 2011.

[28] S. Chen, M. Svedendahl, R. P. V. Duyne, and M. Kll, "Plasmon-enhanced colorimetric elisa with single molecule sensitivity," *Nano Letters*, vol. 11, no. 4, pp. 1826–1830, 2011.

[29] P. Zijlstra, P. M. R. Paulo, and M. Orrit, "Optical detection of single non-absorbing molecules using the surface plasmon resonance of a gold nanorod," *Nature Nanotechnology*, vol. 7, no. 6, pp. 379–382, 2012.

[30] M. A. Beuwer, M. W. J. Prins, and P. Zijlstra, "Stochastic protein interactions monitored by hundreds of single-molecule plasmonic biosensors," *Nano Letters*, vol. 15, no. 5, pp. 3507–3511, 2015.

[31] J. Fritzsche, D. Albinsson, M. Fritzsche, T. J. Antosiewicz, F. Westerlund, and C. Langhammer, "Single particle nanoplasmonic sensing in individual nanofluidic channels," *Nano Letters*, vol. 16, no. 12, pp. 7857–7864, 2016.

[32] A. A. Yanik, M. Huang, O. Kamohara, A. Artar, T. W. Geisbert, J. H. Connor, and H. Altug, "An optofluidic nanoplasmonic biosensor for direct detection of live viruses from biological media," *Nano Letters*, vol. 10, no. 12, pp. 4962–4969, Aug 2010.

[33] M. Zhang, M. Lu, C. Ge, and B. T. Cunningham, "Plasmonic external cavity laser refractometric sensor," *Optics Express*, vol. 22, no. 17, p. 20347, 2014.

[34] M. R. Lee and P. M. Fauchet, "Two-dimensional silicon photonic crystal based biosensing platform for protein detection," *Optics Express*, vol. 15, no. 8, p. 4530, 2007.

[35] S. Mandal, J. M. Goddard, and D. Erickson, "A multiplexed optofluidic biomolecular sensor for low mass detection," *Lab on a Chip*, vol. 9, no. 20, p. 2924, 2009.

[36] H. Inan, M. Poyraz, F. Inci, M. A. Lifson, M. Baday, B. T. Cunningham, and U. Demirci, "Photonic crystals: emerging biosensors and their promise for point-of-care applications," *Chem. Soc. Rev.*, vol. 46, no. 2, pp. 366–388, 2017.

[37] D. Bergstein, E. Ozkumur, A. Wu, A. Yaln, J. Colson, J. Needham, R. Irani, J. Gershoni, B. Goldberg, and C. Delisi et al., "Resonant cavity imaging: A means toward high-throughput label-free protein detection," *IEEE Journal of Selected Topics in Quantum Electronics*, vol. 14, no. 1, pp. 131–139, 2008.

[38] E. Kim, M. D. Baaske, and F. Vollmer, "Towards next-generation label-free biosensors: Recent advances in whispering gallery mode sensors," *Lab Chip*, vol. 17, no. 7, pp. 1190–1205, 2017.

[39] K. D. Heylman, N. Thakkar, E. H. Horak, S. C. Quillin, C. Cherqui, K. A. Knapper, D. J. Masiello, and R. H. Goldsmith, "Optical microresonators as single-particle absorption spectrometers," *Nature Photonics*, vol. 10, no. 12, pp. 788–795, Jul 2016.

[40] H. M. Doeleman, E. Verhagen, and A. F. Koenderink, "Antennacavity hybrids: Matching polar opposites for purcell enhancements at any linewidth," *ACS Photonics*, vol. 3, no. 10, pp. 1943–1951, 2016.

[41] F. Ruesink, H. M. Doeleman, R. Hendrikx, A. F. Koenderink, and E. Verhagen, "Perturbing open cavities: Anomalous resonance frequency shifts in a hybrid cavity-nanoantenna system," *Physical Review Letters*, vol. 115, no. 20, Nov 2015.

[42] M. A. Santiago-Cordoba, S. V. Boriskina, F. Vollmer, and M. C. Demirel, "Nanoparticle-based protein detection by optical shift of a resonant microcavity," *Applied Physics Letters*, vol. 99, no. 7, p. 073701, 2011.

[43] J. D. Swaim, J. Knittel, and W. P. Bowen, "Detection limits in whispering gallery biosensors with plasmonic enhancement," *Applied Physics Letters*, vol. 99, no. 24, p. 243109, Dec 2011.

[44] V. R. Dantham, S. Holler, C. Barbre, D. Keng, V. Kolchenko, and S. Arnold, "Label-free detection of single protein using a nanoplasmonic-photonic hybrid microcavity," *Nano Letters*, vol. 13, no. 7, pp. 3347–3351, Oct 2013.

[45] J. Yang and L. Guo, "Optical sensors based on active microcavities," *IEEE Journal of Selected Topics in Quantum Electronics*, vol. 12, no. 1, pp. 143–147, 2006.

[46] H. T. Beier, G. L. Cot, and K. E. Meissner, "Whispering gallery mode biosensors consisting of quantum dot-embedded microspheres," *Annals of Biomedical Engineering*, vol. 37, no. 10, pp. 1974–1983, 2009.

[47] E. Nuhiji and P. Mulvaney, "Detection of unlabeled oligonucleotide targets using whispering gallery modes in single, fluorescent microspheres," *Small*, vol. 3, no. 8, pp. 1408–1414, Mar 2007.

[48] L. He, a. K. Ozdemir, J. Zhu, W. Kim, and L. Yang, "Detecting single viruses and nanoparticles using whispering gallery microlasers," *Nature Nanotechnology*, vol. 6, no. 7, pp. 428–432, 2011.

[49] A. Yang, T. B. Hoang, M. Dridi, C. Deeb, M. H. Mikkelsen, G. C. Schatz, and T. W. Odom, "Real-time tunable lasing from plasmonic nanocavity arrays," *Nature Communications*, vol. 6, p. 6939, 2015.

[50] M. Lu, S. S. Choi, U. Irfan, and B. T. Cunningham, "Plastic distributed feedback laser biosensor," *Applied Physics Letters*, vol. 93, no. 11, pp. 111–113, 2008.

[51] M. Lu, S. S. Choi, C. J. Wagner, J. G. Eden, and B. T. Cunningham, "Label free biosensor incorporating a replica-molded, vertically emitting distributed feedback laser," *Applied Physics Letters*, vol. 92, no. 26, p. 261502, 2008.

[52] C. Ge, M. Lu, W. Zhang, and B. T. Cunningham, "Distributed feedback laser biosensor incorporating a titanium dioxide nanorod surface," *Applied Physics Letters*, vol. 96, no. 16, p. 163702, 2010.

[53] K. Watanabe, Y. Kishi, S. Hachuda, T. Watanabe, M. Sakemoto, Y. Nishijima, and T. Baba, "Simultaneous detection of refractive index and surface charges in nanolaser biosensors," *Applied Physics Letters*, vol. 106, no. 2, p. 021106, Dec 2015.

[54] Y. Akahane, T. Asano, B.-S. Song, and S. Noda, "High-q photonic nanocavity in a two-dimensional photonic crystal," *Nature*, vol. 425, no. 6961, pp. 944–947, 2003.

[55] J.-N. Liu, M. V. Schulmerich, R. Bhargava, and B. T. Cunningham, "Sculpting narrowband fano resonances inherent in the large-area mid-infrared photonic crystal microresonators for spectroscopic imaging," *Optics Express*, vol. 22, no. 15, p. 18142, 2014.

[56] N. Ganesh, W. Zhang, P. C. Mathias, E. Chow, J. A. N. T. Soares, V. Malyarchuk, A. D. Smith, and B. T. Cunningham, "Enhanced fluorescence emission from quantum dots on a photonic crystal surface," *Nature Nanotechnology*, vol. 2, no. 8, pp. 515–520, 2007.

[57] S. L. Chuang, *Physics of Photonic Devices*. John Wiley, 2009.

[58] W. Zhang, S.-M. Kim, N. Ganesh, I. D. Block, P. C. Mathias, H.-Y. Wu, and B. T. Cunningham, "Deposited nanorod films for photonic crystal biosensor applications," *Journal of Vacuum Science and Technology A: Vacuum, Surfaces, and Films*, vol. 28, no. 4, pp. 996–1001, 2010.

[59] H.-Y. Wu, W. Zhang, P. C. Mathias, and B. T. Cunningham, "Magnification of photonic crystal fluorescence enhancement via TM resonance excitation and TE resonance extraction on a dielectric nanorod surface," *Nanotechnology*, vol. 21, no. 12, p. 125203, Feb 2010.

[60] W. Zhang and B. T. Cunningham, "Fluorescence enhancement by a photonic crystal with a nanorod-structured high index layer," *Applied Physics Letters*, vol. 93, no. 13, p. 133115, 2008.

[61] M. M. Hawkeye and M. J. Brett, "Glancing angle deposition: Fabrication, properties, and applications of micro- and nanostructured thin films," *Journal of Vacuum Science and Technology A: Vacuum, Surfaces, and Films*, vol. 25, no. 5, p. 1317, 2007.

[62] A. Jane, R. Dronov, A. Hodges, and N. H. Voelcker, "Porous silicon biosensors on the advance," *Trends in Biotechnology*, vol. 27, no. 4, pp. 230–239, 2009.

[63] J. T. Verdeyen, *Laser Electronics*. Prentice Hall, 1995.

[64] S. Kita, S. Hachuda, S. Otsuka, T. Endo, Y. Imai, Y. Nishijima, H. Misawa, and T. Baba, "Super-sensitivity in label-free protein sensing using a nanoslot nanolaser," *Optics Express*, vol. 19, no. 18, p. 17683, 2011.

[65] J. Homola and M. Piliarik, "Surface plasmon resonance (spr) sensors," *Springer Series on Chemical Sensors and Biosensors Surface Plasmon Resonance Based Sensors*, pp. 45–67, 2006.

[66] W. Zhou and T. W. Odom, "Tunable subradiant lattice plasmons by out-of-plane dipolar interactions," *Nature Nanotechnology*, vol. 6, no. 7, pp. 423–427, 2011.

[67] F. D. Angelis, M. Patrini, G. Das, I. Maksymov, M. Galli, L. Businaro, L. C. Andreani, and E. D. Fabrizio, "A hybrid plasmonicphotonic nanodevice for label-free detection of a few molecules," *Nano Letters*, vol. 8, no. 8, pp. 2321–2327, 2008.